Dependence of Ice Microphysical Properties on Environmental Parameters: Results from HAIC-HIWC Cayenne Field Campaign

Yachao Hu, Greg M. Mcfarquhar, Wei Wu, Yongjie Huang, Alfons Schwarzenboeck, Alain Protat, Alexei Korolev, Robert M. Rauber, Hongqing Wang

Dependence of Ice Microphysical Properties on Environmental Parameters: Results from HAIC-HIWC Cayenne Field Campaign

YACHAO HU,[a,b] GREG M. MCFARQUHAR,[b,c] WEI WU,[b] YONGJIE HUANG,[c,d] ALFONS SCHWARZENBOECK,[e] ALAIN PROTAT,[f] ALEXEI KOROLEV,[g] ROBERT M RAUBER,[h] AND HONGQING WANG[a]

[a] *Department of Atmospheric and Oceanic Sciences, School of Physics, Peking University, Beijing, China*
[b] *Cooperative Institute for Mesoscale Meteorological Studies, University of Oklahoma, Norman, Oklahoma*
[c] *School of Meteorology, University of Oklahoma, Norman, Oklahoma*
[d] *Center for Analysis and Prediction of Storms, University of Oklahoma, Norman, Oklahoma*
[e] *Laboratoire de Météorologie Physique, UCA, CNRS, Aubière, France*
[f] *Australian Bureau of Meteorology, Melbourne, Australia*
[g] *Environment and Climate Change Canada, Toronto, Canada*
[h] *Department of Atmospheric Sciences, University of Illinois at Urbana–Champaign, Urbana, Illinois*

(Manuscript received 20 January 2021, in final form 23 June 2021)

ABSTRACT: High ice water content (HIWC) regions above tropical mesoscale convective systems are investigated using data from the second collaboration of the High Altitude Ice Crystals and High Ice Water Content projects (HAIC-HIWC) based in Cayenne, French Guiana, in 2015. Observations from in situ cloud probes on the French Falcon 20 determine the microphysical and thermodynamic properties of such regions. Data from a 2D stereo probe and precipitation imaging probe show how statistical distributions of ice crystal mass median diameter (MMD), ice water content (IWC), and total number concentration (N_t) for particles with maximum dimension (D_{max}) > 55 μm vary with environmental conditions, temperature (T), and convective properties such as vertical velocity (w), MCS age, distance away from convective peak (L), and surface characteristics. IWC is significantly correlated with w, whereas MMD decreases and N_t increases with decreasing T consistent with aggregation, sedimentation, and vapor deposition processes at lower altitudes. MMD typically increases with IWC when IWC < 0.5 g m^{-3}, but decreases with IWC when IWC > 0.5 g m^{-3} for $-15° \le T \le -5$°C. Trends also depend on environmental conditions, such as the presence of convective updrafts that are the ice crystal source, MMD being larger in older MCSs consistent with aggregation and less injection of small crystals into anvils, and IWCs decrease with increasing L at lower T. The relationship between IWC and MMD depends on environmental conditions, with correlations decreasing with decreasing T. The strength of correlation between IWC and N_t increases as T decreases.

KEYWORDS: Tropics; Cloud microphysics; Convective storms; Ice crystals; Ice particles

1. Introduction

Clouds affect the dynamics and thermodynamics of the troposphere and are a key component in the energy balance and water cycle of Earth. The spatial and temporal distribution of clouds is inhomogeneous, making their representation one of the largest sources of uncertainty in climate models (e.g., Intergovernmental Panel on Climate Change 2013; Chen et al. 2018). Mesoscale convective systems (MCSs), commonly defined as organized clusters of cumulonimbus clouds with contiguous precipitation regions over 100 km on a horizontal scale in at least one direction (Houze 2014; Houze et al. 2019; Markowski and Richardson 2010), are one of the most important types of convective systems on Earth.

Ice crystals found in cirrus and MCSs make important contributions to the radiative budget of Earth. The number distribution function [$N(D)$] is one of the important functions to describe microphysical properties of an ensemble of ice particles; $N(D)$ is also referred to as particle size distribution (PSD) and it allows assessment of total number concentration N_t, ice water content (IWC), mass-weighted terminal velocity v_m, effective radius R_e, and single scattering properties such as extinction β, many of which are prognosed or diagnosed in general circulation models (GCMs). Knowledge of ice crystal particle properties aids in the understanding of cloud microphysical processes and in the development of parameterizations of microphysical processes in GCMs (e.g., Stephens 2005; Jakob and Klein 1999; Sanderson et al. 2008; Jackson et al. 2015). For example, ice crystal fall speed, which is a function of crystal size assumed in ice cloud parameterizations, has a big effect on modeled cloud cover, life cycle, and radiative forcing (Sanderson et al. 2008). Mitchell et al. (2008) found that the GCMs predict a 12% increase in cloud ice amount and a 5.5% increase in cirrus cloud coverage globally when small ice crystals concentrations are increased due to the impact on ice sedimentation rates. Simulations from Boudala et al. (2007) including contributions of crystals with mean effective size less than 150 μm had a net radiative forcing of 2.4 W m^{-2} greater than that of a control case where such contributions were excluded. McFarquhar and Black (2004) and others show knowledge of the size distribution is critical in determining the representation of sedimentation. In addition, knowledge of ice crystal sizes influences vertical profiles of radiative heating that affects the evolution of cloud systems and estimates of cloud radiative forcing

Corresponding author: Greg McFarquhar, mcfarq@ou.edu

DOI: 10.1175/JAS-D-21-0015.1

(e.g., McFarquhar et al. 2000, 2003; Heymsfield and McFarquhar 2002). Trends in how ice crystal properties vary with environmental conditions also give some indications of the microphysical processes that affect their evolution. Thus, knowledge about the controls of ice crystal properties articles can provide both process-oriented understanding of microphysical processes and improved parameterization of such processes for numerical models.

Aircraft measurements of the microphysical properties of tropical anvils generated by convection have been obtained in previous observational campaigns, including the Central Equatorial Pacific Experiment (CEPEX; McFarquhar and Heymsfield 1996), the Texas and Florida Underflights (TEFLUN-A and -B; Gage et al. 1999), the Brazil Large Scale Biosphere–Atmosphere Experiment (LBA; Formenti et al. 2001), the Kwajalein, Marshall Islands Kwajalein Experiment (KWAJEX; Heymsfield et al. 2002; Sobel et al. 2004), the Convection And Moisture Experiment (CAMEX-4; Kakar et al. 2006), the Tropical Cloud Systems and Processes experiment (TCSP; Halverson et al. 2007), the Tropical Warm Pool International Cloud Experiment campaign (TWP-ICE; May et al. 2008), the National Aeronautics and Space Administration (NASA) African Monsoon Multidisciplinary Analysis (NAMMA; e.g., Heymsfield et al. 2009; Cifelli et al. 2010; Lawson et al. 2010; Bouniol et al. 2010; Mascio et al. 2020), and the Tropical Composition, Cloud, and Climate Coupling (TC4; e.g., Jensen et al. 2009; Toon et al. 2010;Lawson et al. 2010). Although prior studies have provided a wealth of cloud probe data for process understanding and parameterization development, only on rare occasions have IWCs larger than $1.5\,\mathrm{g\,m^{-3}}$ been measured, which is used here to designate high-IWC (hereafter HIWC) regions. No distinction is made about the size of particles when defining HIWC regions. Although some previous studies used a threshold of $1.0\,\mathrm{g\,m^{-3}}$ to define HIWC regions (e.g., McFarquhar and Heymsfield 1996; Lawson et al. 1998), HIWC conditions are defined here using a threshold of $1.5\,\mathrm{g\,m^{-3}}$ following the convention used for the HAIC-HIWC experiments (Leroy et al. 2016a, 2017; Strapp et al. 2020, 2021). Typically, measurements of high IWCs are hard to obtain because they are believed to occur close to convective cores where flying can be limited due safety reasons. Further, even when measurements have been made in HIWC regions, the measurements are highly uncertain because probes that measure bulk IWC tend to become saturated at high IWC (Davison et al. 2016; Strapp et al. 2016a) and estimates of IWC based on measured PSDs are highly uncertain without bulk measurements of IWC (e.g., McFarquhar et al. 2007a; Heymsfield et al. 2004; Lawson et al. 2010; Fontaine et al. 2014).

To overcome these difficulties, an international multiagency collaboration called the High Altitude Ice Crystals (Dezitter et al. 2013) and High Ice Water Content (Strapp et al. 2016b) projects (HAIC-HIWC) organized multiple field campaigns to make microphysical measurements of HIWC conditions to investigate processes responsible for their occurrence. The particular focus of these experiments was to investigate regions with HIWC that were mainly composed of small crystals (area equivalent diameters $< 300\,\mu\mathrm{m}$) that had equivalent radar reflectivity values less than 30 dBZ and often lower than 20 dBZ for pilot X-band radar data (e.g., Lawson et al. 1998; Mason et al. 2006; Bravin et al. 2015; Fridlind et al. 2015; Wolde et al. 2016; Leroy et al. 2017). The effort consisted of three focused field campaigns in February 2014 (HAIC-HIWC: Darwin, Australia; Leroy et al. 2017), May 2015 (HAIC-HIWC: Cayenne, French Guiana; Dezitter et al. 2013; Strapp et al. 2016b), and August 2015 (HAIC-RADAR: Florida; Yost et al. 2018; Ratvasky et al. 2019). An overview of the total water content (TWC) and PSD microphysical results from these three campaigns, as applied to aviation regulatory issues, has been provided by Strapp et al. (2020). The data considerably extend those previously collected in cirrus outflows of tropical convection because of the focus on HIWC conditions and because a new bulk probe, the isokinetic evaporator probe (IKP2), was used to make more accurate measures of bulk mass in HIWC conditions.

Previous analysis of data collected during the Darwin campaign has shown that some HIWC (defined as IWC $> 1.5\,\mathrm{g\,m^{-3}}$ irrespective of the sizes of particles) regions are indeed characterized by numerous small ice crystals. In particular, Leroy et al. (2017) found that in most cases ice crystals with area equivalent diameters (D_a) between 250 and 500 μm dominated the mass in the HIWC regions, similar to the findings of Fridlind et al. (2015) who used Airbus data to show HIWC regions had median D_a of 200–300 μm. However, in two other HAIC-HIWC cases the HIWC regions were dominated by ice crystals with D_a between 400 and 800 μm and up to 2 mm. Yost et al. (2018) used HAIC-HIWC data from all three campaigns, combined with geostationary satellite imager data, to develop a better climatology of HIWC conditions, showing the probability of HIWC occurrence depends on the proximity to an overshooting convective cloud top, the infrared brightness temperature at the tropopause and the daytime cloud optical depth.

Although these studies have provided a foundation on where HIWC regions occur, they are still not sufficient to explain the variability of ice properties. For example, strong vertical motions may transport ice crystal particles and tend to sort particles by size (Leroy et al. 2016a), different physical processes for different regions in MCS lead to different rain intensity at the surface and different radiative properties (Houze 2004), and Bouniol et al. (2016) found the amounts of hydrometeors that are lifted to high altitudes vary with MCS life cycle and vary for MCSs over three kinds of underlying surface characteristics (defined as whether the surface was land, ocean, or coastline). Thus, examining the dependence of cloud properties on environmental conditions yields information about physical processes that are related to the production and distribution of ice crystal particles. Thus, the effect of these environmental conditions and properties of MCS (e.g., vertical motions, underlying surface characteristics defined as whether the surface was land, ocean or coastline, age of convective system, and different regions in a convective system) are examined to see how they affect the properties of ice crystals and the frequency of occurrence of HIWC conditions dominated by small ice crystals.

Therefore this paper uses data obtained during the second HAIC-HIWC campaign conducted from 9 to 29 May 2015 out

TABLE 1. Overview of the 17 flights through 14 MCSs during the HAIC-HIWC Cayenne campaign. Peak IWC values derived from IKP2 measurements at 5-s resolution. A double bar indicates there are no data at this temperature level.

Flight number (time and date)	Max IWCs at different flight levels (g m^{-3})			Underlying surface	Time and date		Lifetime (h)
	−15° to −5°C	−35° to −25°C	−50° to −40°C		Initial time	Dissipation time	
F10 (1903–2121 UTC 10 May)	—	—	2.1	Continental	1815 UTC 10 May	0045 UTC 11 May	6.5
F11 (2020–2226 UTC 12 May)	—	1.3	0.7	Continental	1715 UTC 12 May	1115 UTC 13 May	18
F12 (1417–1715 UTC 14 May)	—	0.4	—	Coastal	0715 UTC 14 May	1915 UTC 14 May	12
F13 (0835–1209 UTC 15 May)	3.9	3.1	2.1	Oceanic	0215 UTC 15 May	2115 UTC 15 May	19
F14 (0823–1154 UTC 16 May)	1.0	3.3	—	Oceanic	0145 UTC 16 May	1915 UTC 17 May	41.5
F15 (1559–1833 UTC 16 May)	2.9	2.1	—	Continental			
F16 (1927–2220 UTC 18 May)	2.2	2.5	1.5	Oceanic	0345 UTC 18 May	0215 UTC 19 May	22.5
F17 (1419–1727 UTC 19 May)	—	2.3	1.9	Oceanic	0145 UTC 19 May	2215 UTC 20 May	44.5
F18 (0914–1244 UTC 23 May)	—	2.6	—	Oceanic	0245 UTC 23 May	2245 UTC 23 May	20
F19 (1523–1859 UTC 23 May)	3.1	1.8	2.3	Oceanic			
F20 (0851–1208 UTC 24 May)	3.6	3.2	2.7	Oceanic	2245 UTC 23 May	1545 UTC 24 May	17
F21 (1907–2240 UTC 25 May)	—	2.6	2.6	Continental	1445 UTC 25 May	1415 UTC 26 May	23.5
F22 (0833–1159 UTC 26 May)	3.7	3.1	3.5	Oceanic	2115 UTC 25 May	0615 UTC 27 May	33
F23 (1310–1551 UTC 26 May)	3.2	1.4	2.4	Oceanic			
F24 (0827–1206 UTC 27 May)	3.0	3.4	—	Oceanic	0515 UTC 27 May	2345 UTC 27 May	18.5
F25 (1925–2253 UTC 28 May)	2.3	1.9	1.5	Continental	1215 UTC 28 May	0715 UTC 29 May	19
F26 (0847–1206 UTC 29 May)	3.1	2.6	3.0	Coastal	2245 UTC 28 May	2115 UTC 29 May	22.5

of Cayenne, French Guiana, to investigate how the distributions of IWC, N_t, and mass median diameters (MMD) vary with environmental conditions such as temperature (T), vertical velocity (w), underlying surface characteristics, the distance away from the peak of the convective core (L), the age of the convective system, and the brightness temperature difference between two channels of 6.8 and 10.8 μm ($BTD_{6.8–10.8\mu m}$) that is correlated with the strength of convection system (e.g., Wu et al. 2016). Further, the dependence of MMD on IWC and the relationship between N_t and IWC as a function of these conditions are examined. The microphysical properties of the HIWC regions are also contrasted with observations obtained in regions without HIWCs. The rest of the paper is organized as follows. Section 2 describes the HAIC-HIWC dataset and methodology used to process the data. An example of a HIWC event is presented in section 3. Investigations of how the statistical distributions of MMD, IWC, and N_t vary with environmental conditions are shown in section 4. Section 5 summarizes the results and offers directions for future research.

2. Dataset and methodology

The second HAIC-HIWC flight campaign was based out of Cayenne (French Guiana) during 9–25 May 2015. Three aircraft were used: 1) the French Falcon 20, equipped with in situ cloud probes, flew in convective systems at varying temperatures; 2) the National Research Council (NRC) Canadian Convair 580, equipped with in situ cloud probes and the NRC Airborne W- and X-band (NAWX) Doppler dual-polarization radars (Wolde and Pazmany 2005; Nguyen et al. 2019), flew mainly at a temperature level of −10°C; and 3) the Honeywell B757, flew outside of clouds at the altitudes the Falcon 20 was flying to evaluate new pilot radar detection algorithms of HIWC. Only the in situ data acquired using the Falcon 20 are analyzed in this study to avoid any complications with different calibrations, probe functionally or processing algorithms that may affect the comparison of microphysical properties (McFarquhar et al. 2017). Comparing data from the same probe in different conditions is the most robust way to detect subtle differences in cloud properties.

Seventeen research flights, designated F10 through F26 were performed with the French Falcon 20 and are summarized in Table 1. The cloud measurements are sorted into three temperature levels: −10°, −30°, and −45°C as the flight strategies were mainly designed to acquire statistics on HIWCs at these altitudes. Three types of convective systems were sampled during HAIC-HIWC: two flights (F12, F26) sampled coastal convective systems; five flights (F10, F11, F15, F21, F25) sampled continental convective systems; and ten flights (F13, F14, F16, F17, F18, F19, F20, F22, F23, F24) sampled oceanic convective systems. The classification of these systems is defined according to the surface underlying the aircraft at the time of sampling.

a. Airborne instrumentation

The in situ instruments mounted on the Falcon 20 include a cloud droplet probe version 2 (CDP-2), which nominally measures the PSDs, of cloud droplets between 2 and 50 μm from forward scattering of laser light of 785 nm wavelength (Lance et al. 2010), a 2D stereo probe (2D-S) with 128 photodiodes and a photodiode resolution of 10 μm, and a precipitation imaging probe (PIP) with 64 photodiodes and a photodiode resolution of 100 μm. The 2D-S and PIP nominally measure hydrometers with sizes between 10–1280 and 100–6400 μm, respectively, by measuring particle size and shape from an array of photodiode detectors attached to fast

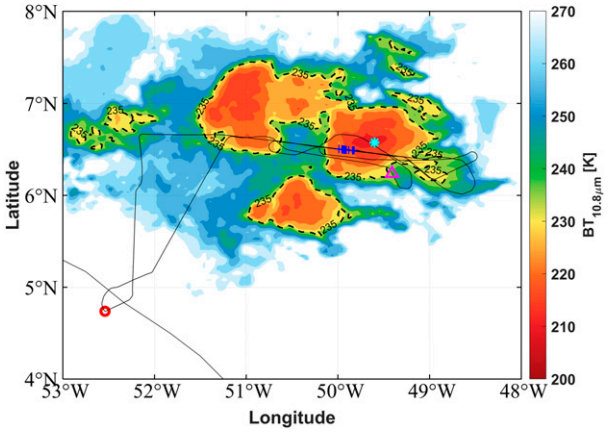

FIG. 1. *GOES-13* measured brightness temperature ($BT_{10.8\mu m}$) at 1115:00 UTC 15 May 2015 with flight track of Falcon 20 overlaid with black line for flight 13. The black dashed line shows the temperature contour line at 235 K. Red circle indicates location of Cayenne (4.74°N, 52.5°W), blue points indicate where IKP2 IWC $> 1.5\,g\,m^{-3}$ and MMD $< 400\,\mu m$ between $-50° \le T \le -40°C$, magenta triangle and cyan asterisk ($BT_{10.8\mu m}$ = 213.6 K) denote location of aircraft and of MCS convective core at 1115:00 UTC, respectively.

response electronics (Lawson et al. 2006; Baumgardner et al. 2011, 2017). All particle probes were equipped with anti-shattering tips to mitigate the effect of ice particle shattering on measurements (Korolev et al. 2013a). The primary measurement of TWC, which is the sum of the IWC and liquid water content (LWC), was made with IKP2 specially designed for this project for the high-TWC environmental conditions (Davison et al. 2016; Strapp et al. 2016a). Secondary TWC measurements from a Science Engineering Associates (SEA) Robust hot wire TWC probe (Strapp et al. 2008; Grandin et al. 2014) provided backup and corroboration of IKP2 functionality. A Rosemount Icing Detector (Baumgardner and Rodi, 1989; Claffey et al. 1995; Cober et al. 2001), the CDP-2, and a LWC probe from SEA were used in combination to identify mixed-phase conditions and estimate LWC when at sufficient levels. A multibeam 95-GHz Doppler cloud radar (RAdar SysTem Airborne, RASTA) provided reflectivity and Doppler velocity (Protat et al. 2009; Leroy et al. 2016a). Temperature was measured by Rosemount 102 probe with an uncertainty of ±1°C. Vertical velocity was measured by Rosemount 858 five-hole pressure probe and transducers with an uncertainty of $\pm 0.3\,m\,s^{-1}$ (Hartmann et al. 2018; Strapp et al. 2020). These two probes were installed on the French Falcon 20 and operated by the Service des Avions Francais Instrumentes pour la Recherche en Environnement (SAFIRE).

b. Data processing

1) Ice water content

The IKP2, specifically developed to measure the high IWCs expected during the HAIC-HIWC campaigns, was designed to measure condensed water contents up to $10\,g\,m^{-3}$ at airspeeds of $200\,m\,s^{-1}$ with an accuracy of at least 20% (Davison et al. 2008, 2016; Strapp et al. 2016a). Its isokinetic flow control ensures that liquid and ice particles are sampled at near unit efficiency without significant ice mass loss that is associated with bulk TWC hot-wire probes. TWC is estimated as the difference between the evaporated condensed water and background humidity. By subtracting the best estimate of humidity, assumed to be ice saturation to follow the method of Strapp et al. (2016a), data were generated for 5-s centered averages at 1-s spacing. The TWC is identical to IWC in the absence of liquid water, whose presence is inferred from a Rosemount icing detector (Baumgardner and Rodi 1989). Cloud segments where the Rosemount icing detector frequency was decreasing and was lower than 40 kHz (Mazin et al. 2001) or N_t detected by CDP-2 larger than $10\,cm^{-3}$ (Lance et al. 2010; Ding et al. 2020) identified the presence of LWC and occurred only 0.81% of the time. These data were removed from subsequent analysis to focus only on ice-phase conditions. To remove tenous clouds and consistent with the focus on HIWC clouds, only data with IWC $\ge 0.1\,g\,m^{-3}$ were used here. Maximum IWCs obtained by the IKP2 in Cayenne at different temperature levels for each flight are listed in Table 1.

TABLE 2. Number of 5-s samples acquired in different environmental conditions.

	Flight temperature levels			
	−15° to −5°C	−35° to −25°C	−50° to −40°C	Total
MCS types				
Oceanic	2619	3041	1751	7411
Coastal	290	352	904	1546
Continental	450	989	1943	3382
Vertical motions				
Updrafts	146	249	214	609
Stratiform	3181	4024	4115	11 320
Downdrafts	32	109	269	410
MCS age				
<6 h	120	733	1196	2049
6–12 h	1173	2294	1334	4801
>12 h	2066	1355	2068	5489
Distance from convective core				
≤50 km	902	1493	1293	3688
50–100 km	548	1064	1021	2633
100–200 km	942	989	1434	3365
>200 km	967	836	850	2653
$BTD_{6.8-10.8\mu m}$				
<−3 K	302	861	535	1698
−3 to −1 K	1478	2474	2072	6024
>−1 K	1579	1047	1991	4617
Total	3359	4382	4598	12 339

2) Particle size distributions

Composite PSDs were derived from the 2D-S and PIP data, covering particle maximum dimensions (D_{max}) from 55 to 12 845 μm at 10-μm resolution and representing 5-s averages (Leroy et al. 2017). The 5-s average represents a trade-off

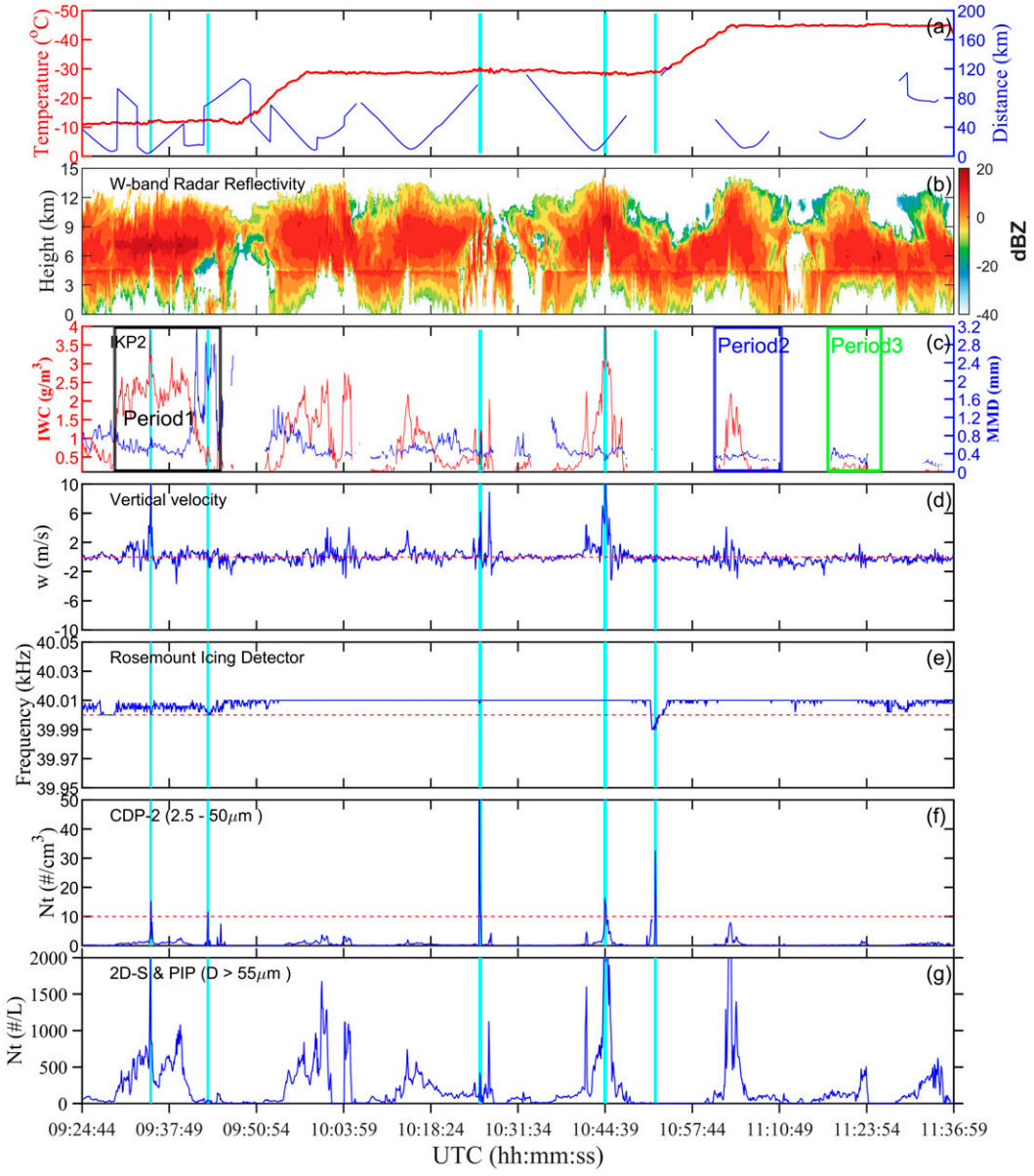

FIG. 2. Time series of (a) temperature at flight altitude (red line), distance away from convective core (blue line, times when aircraft flew out of MCS not shown), (b) W-band radar reflectivity from the multibeam 95-GHz Doppler cloud radar mounted on Falcon 20, (c) IWC from IKP2 (red line) and MMD (blue line), (d) vertical velocity (w), (e) Rosemount icing detector frequency (blue line) with threshold of 40 kHz indicating presence of supercooled liquid water (red line), (f) total number concentration (N_t) with diameter between 2.5 and 50 μm measured by CDP-2 (blue line) and threshold of 10 cm^{-3} corresponding to liquid water (red line), and (g) N_t from composite 2D-S ($D_{max} > 55\ \mu$m) and PIP size distribution for the 0924:44–1136:59 UTC 15 May 2015 flight leg. Shaded gray boxes represent locations of Rosemount icing detector frequency less than 40 kHz; shaded cyan boxes indicated N_t measured by CDP-2 larger than 10 cm^{-3}.

between large numbers of particles for statistically significant sampling and fine resolution to resolve small-scale features of clouds (McFarquhar et al. 2007b). The best estimates of PSDs obtained using processing algorithms of Environment and Climate Change Canada and of the Université Blaise Pascal compared well against PSD generated using the University of Illinois/Oklahoma Optical Probe Processing Software (McFarquhar et al. 2017) for two 3-min periods from HAIC-HIWC, suggesting uncertainties in the processing algorithms were not affecting the derived PSDs. The processing algorithms assumed the sample area depended on the particle dimension along the photodiode array, included corrections for out-of-focus particles (Korolev 2007), and treated partially imaged particles following the approach of Heymsfield and

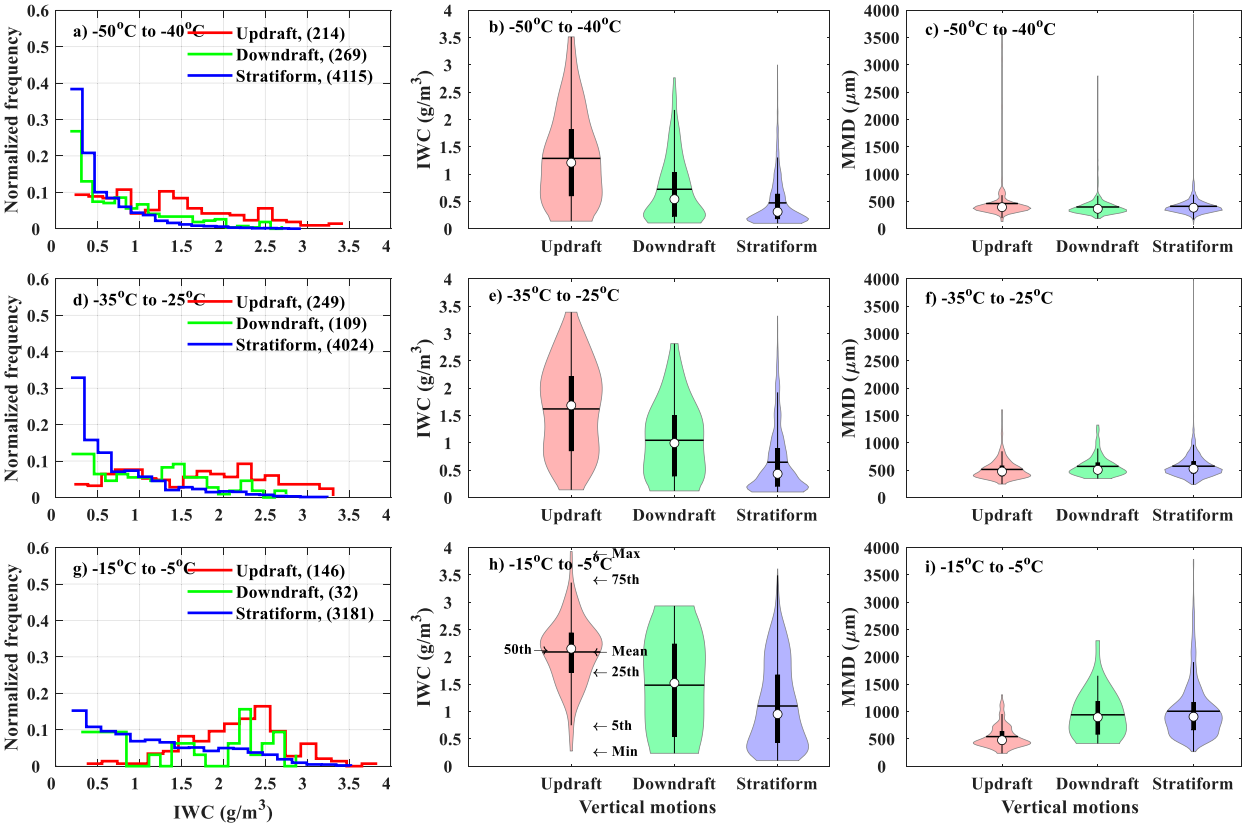

FIG. 3. Normalized frequency of occurrence of IWC for updrafts, downdrafts and stratiform regions for temperature levels: (a) −50° to −40°C, (d) −35° to −25°C, and (g) −15° to −5°C. Red represents updrafts, green represents downdrafts, and blue represents stratiform regions. Number of data points for each condition shown in legend. (b),(e),(h) Violin plots of IWC for updrafts, downdrafts, and stratiform regions for each T. Top and bottom of the violin plot indicate maximum and minimum, respectively. Black boxplots show 5th, 25th, 50th (white point), 75th, and 95th percentile of distribution. Horizontal black line indicates mean value. Width of shaded area represents proportion of data located there. (c),(f),(i) As in (a), (d), and (g), but for MMD.

Parrish (1978). PSDs were generated as functions of $D_{\max}$, the length along the photodiode array and D_a. In this study, $D_{\max}$ is used to represent the particle dimension for easier comparison with prior studies and model parameterizations. Contributions from particles with $D_{\max} < 55\,\mu$m are not included in the analysis because of large uncertainties associated with a size-dependent and poorly defined sample area (Baumgardner and Korolev 1997; Korolev et al. 1998), and the possible inclusion of shattered artifacts not filtered by processing algorithms because of the higher airspeeds (Field et al. 2006; Korolev and Field 2015). Previous studies have shown that PSDs from such sizes are highly uncertain (e.g., Jackson et al. 2015; McFarquhar et al. 2017). Data obtained by the CDP-2 are not considered here because the interpretation of its measurements in ice clouds is highly uncertain (McFarquhar et al. 2007a). The IWC and vertical velocity data were sorted into 5-s periods to match the integration period used for the PSD data.

3) MASS-SIZE DISTRIBUTION

Particle mass is not measured by the imaging probes. A mass–dimensional (m–$D_{\max}$) relation was used to estimate IWC from a PSD, where

$$m = \alpha D_{\max}^{\beta}, \tag{1}$$

with β varying in time according to measured crystal morphology following Leroy et al. (2016b, 2017), and α determined by forcing agreement between the IWC measured by the IKP2 and that derived from the PSD. The IKP2 was mounted on the left wing and PSD probes (2D-S and PIP) were mounted on the right wing of French Falcon 20 (the sight direction is from a vantage in front of and looking toward the plane; Strapp et al. 2020). The mean airspeed of the aircraft is 170 m s^{-1} and IWCs measured by IKP2 vary by about 0.7% in 1 s. The spatial scale corresponding to 1 s (170 m) is much larger than the spatial scale corresponding to the distance between the probes, thus the uncertainty caused by the distance between the probes is much less than 0.7%. Further, the same particles are not sampled even if the probes are right next to each other. Thus, this factor was not included when calculating MMD due to the distance between probes is not a large source of uncertainty. The values of α (median: 0.0038) and β (median: 2.05) in the m–$D_{\max}$ relation are similar to those derived from previous studies, for example, $\alpha = 0.0070$ and $\beta = 2.2$ for Heymsfield et al. (2010), $\alpha = 0.002\,57$ and $\beta = 2.0$ for Cotton et al. (2013),

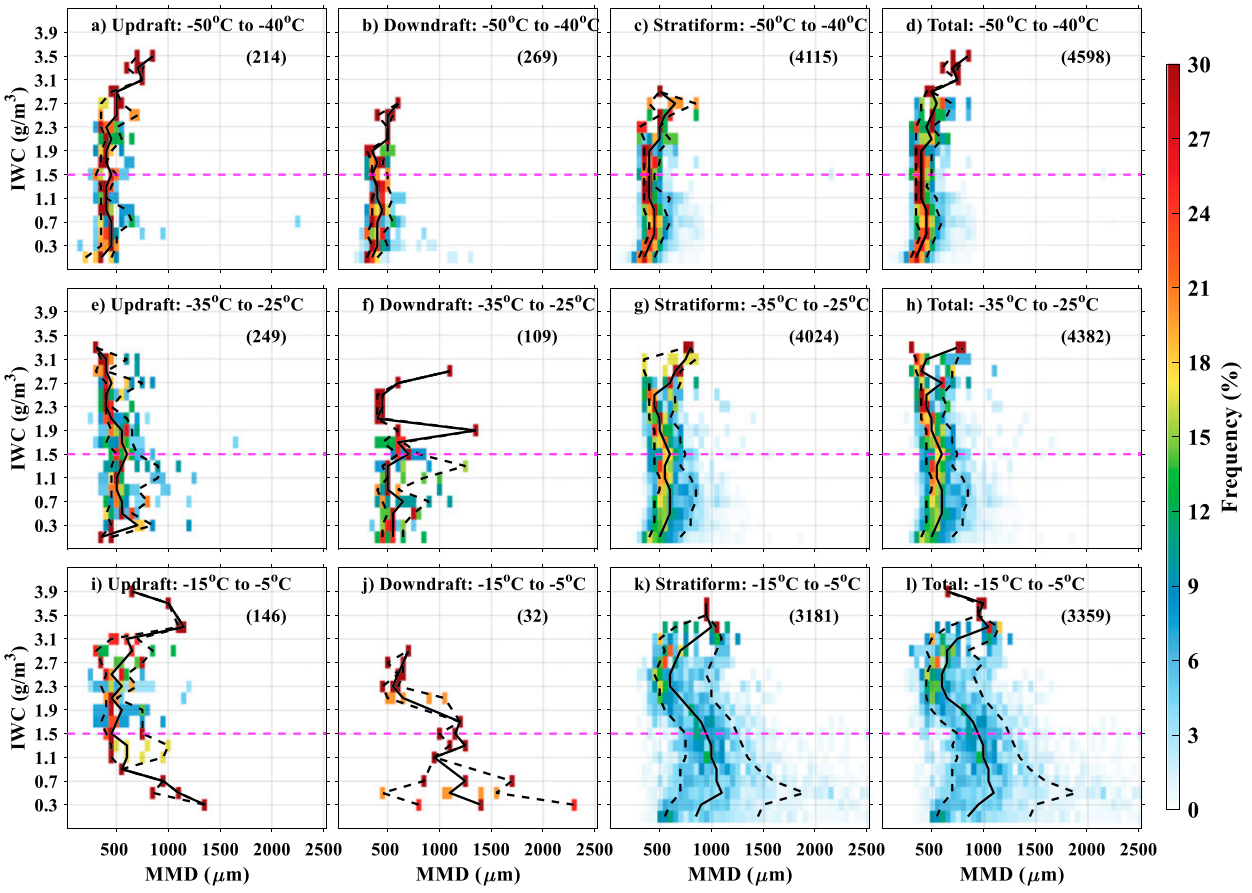

FIG. 4. Normalized frequency of MMD for each IWC range for (a) updrafts, (b) downdrafts, (c) stratiform regions, and (d) all three combined for temperatures between −50° and −40°C. (e)–(h) As in (a)–(d), but for temperatures from −35° to −25°C. (i)–(l) As in (a)–(d), but for temperatures from −15° to −5°C. For each panel, the middle solid line indicates the 50th percentile, whereas the left and right dashed lines represent 15th and 85th MMDs, respectively. The magenta dashed horizontal lines mean IWC = 1.5 g m^{-3}. Numbers in parentheses give number of sample data points.

$\alpha = 0.0054$ and $\beta = 2.05$ for Fontaine et al. (2014), where $D_{\max}$ is in cm and α is in g cm$^{-\beta}$. Detailed flow of calculation for α and β is described by Leroy et al. (2016b) and Strapp et al. (2020). MMD was derived as the dimension for which half the mass is contained in smaller particles and half in larger particles to follow previous studies (e.g., Fridlind et al. 2015; Leroy et al. 2017; Stanford et al. 2017; Strapp et al. 2020), and is represented numerically as follows:

$$\int_0^{\mathrm{MMD}} \alpha D_{\max}^{\beta} N(D_{\max})\, dD_{\max} = \int_{\mathrm{MMD}}^{\infty} \alpha D_{\max}^{\beta} N(D_{\max})\, dD_{\max} = \frac{1}{2}\mathrm{IWC}. \quad (2)$$

Besides the influence of the m–$D_{\max}$ relationship, MMD is mainly controlled by the PSDs themselves. Sensitivity studies demonstrate that MMD is relatively insensitive to even very large increases in the concentrations of the smallest particle sizes (e.g., $D_a < 50\,\mu$m) (Leroy et al. 2017). The omission of particles with $D_{\max} < 55\,\mu$m changed the calculated MMD by 0.76% on average compared to including these points. The mean absolute differences between the MMDs computed from different size definitions ($D_{\max}$, the area equivalent diameter, the length along the photodiode array, and the mean chord length) vary between 30 and 50 μm (Leroy et al. 2016b). The MMD gives a good indication of whether or not the PSDs are dominated by small ice crystals.

4) SATELLITE IMAGE DATA

GOES-13 data are used to identify individual convective systems, and to determine the location of the aircraft within each MCS (e.g., the distance away from a convective core), and the age of the convective system. The *GOES-13* data at spectral channels of 6.8 and 10.8 μm with a temporal resolution of 30 min are used here. The spatial resolution is about 4 km and the data are available over the domain of (0°–10°N, 45°–60°W) where the aircraft flew during the Cayenne campaign (https://doi.org/10.5065/D6NC5ZX6).

c. *Methodology*

1) METHOD OF IDENTIFYING MCS AND AGE OF MCS

The brightness temperature (BT) threshold used to define points inside MCSs has varied substantially in prior studies,

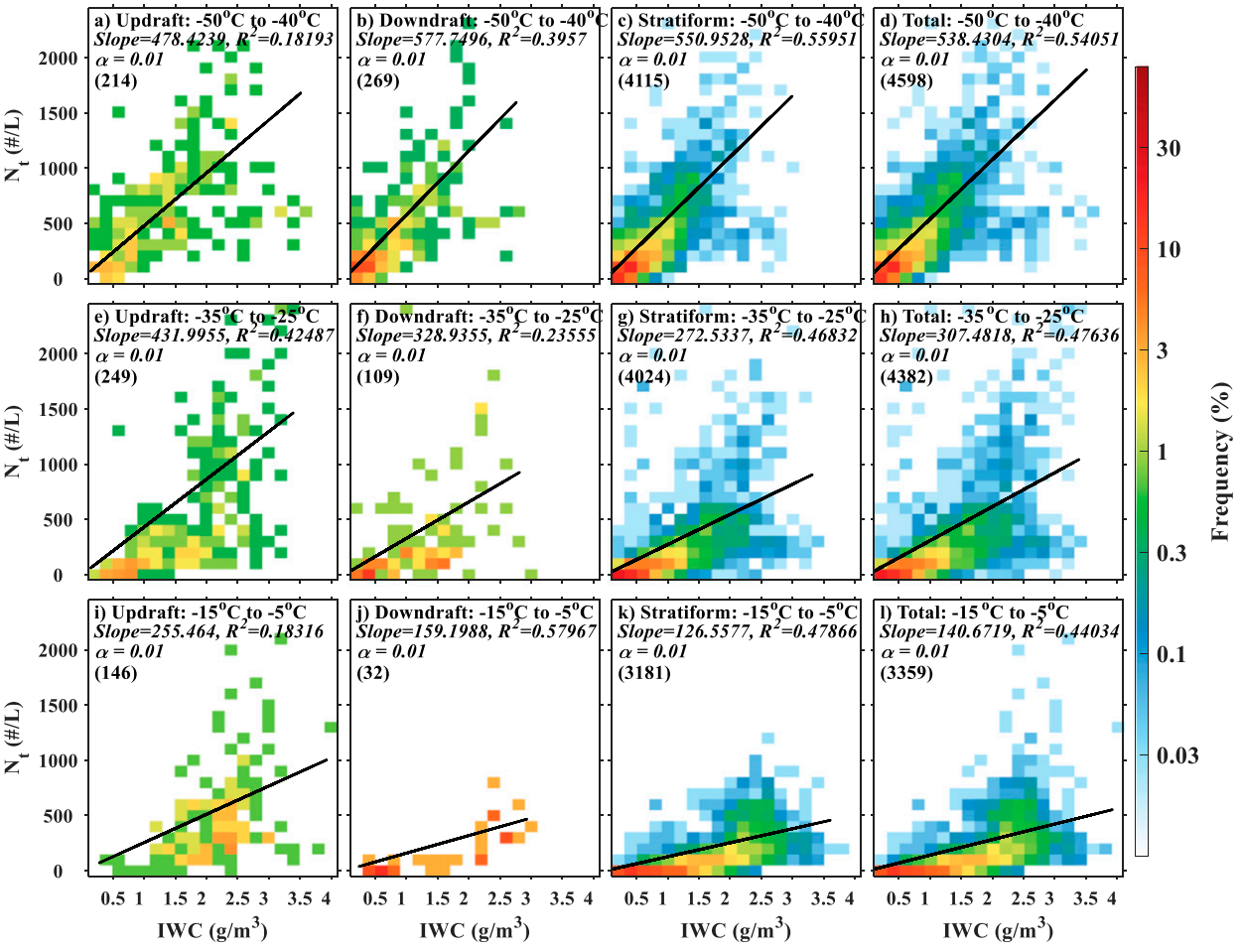

FIG. 5. Normalized two-dimensional frequency distributions of N_t and IWC for (a) updrafts, (b) downdrafts, (c) stratiform regions, and (d) all three combined for temperatures from −50° to −40°C. (e)–(h) As in (a)–(d), but for temperatures from −35° to −25°C. (i)–(l) As in (a)–(d), but for temperatures from −15° to −5°C. For each panel, black line gives best fit. Slope of fit line, coefficient of determination R^2, and significance level (α) are shown. Numbers in parentheses represent number of sample data points.

ranging from 208 to 258 K (e.g., Hodges and Thorncroft 1997; Machado et al. 1998; Ai et al. 2016; Rafati and Karimi 2017). Arkin and Meisner (1987) found that cloud tops with BT < 235 K were associated with tropical rainfall so that a threshold of 235 K has since been used to identify points contained within MCSs (Laurent et al. 2002; Vila et al. 2008). For this study, convective cloud candidates were first determined according to the definition of an MCS, which is defined to occur when the major axis of an area with the BT of the 10.8-μm channel ($BT_{10.8\mu m}$) < 235 K is longer than 100 km (Kolios and Feidas 2010; Chen et al. 2018). As the resolution of *GOES-13* is about 4 km, this means the number of pixels along the major axis of the MCS identified area should be larger than 25. The function "boundaries" in MATLAB (Gonzalez et al. 2004) was used to identify each MCS and connection needs to satisfy the condition that eight pixels are connected. If an identified region with temperature below 235 K is peanut shaped with a very thin connection at the middle, it still satisfies this standard, and the major axis would be the full length of the peanut regardless of how narrow the connection is. Second, the time of MCS formation was defined as the time when at least one pixel of $BT_{10.8\mu m}$ became smaller than 235 K, determined by examining the trajectory of the convective clouds' previous development visually. Third, the time of dissipation was defined as the time when $BT_{10.8\mu m}$ of all points in the system became greater than 235 K by examining the trajectory of the convective clouds' subsequent development visually. At the initial time and time of dissipation, the principal axes of the MCS does not need to be greater than 100 km. All MCSs in this study are confined to the region (0°–10°N, 45°–60°W). The period from the initial time to the dissipating time is defined as the total lifetime of the convective system and the age of MCS can be calculated by using the actual time of the observation minus the initial time. Fourteen convective systems were identified for times corresponding to Falcon 20 observations and their properties are summarized in Table 1. The average lifetime of the 14 MCSs sampled was 22.6 h and the average age of the systems sampled was 10.6 h.

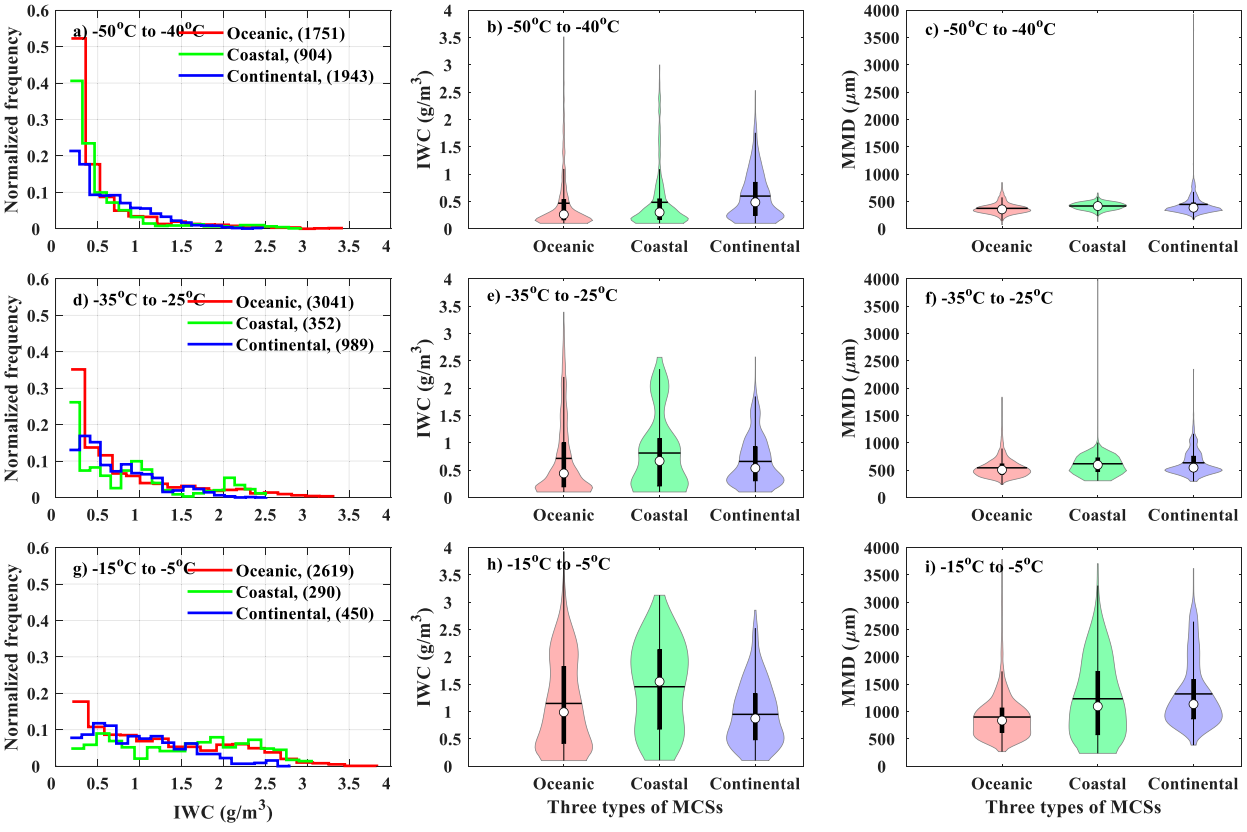

FIG. 6. As in Fig. 3, but for MCSs over different surfaces (oceanic, coastal, and continental) rather than for updrafts, downdrafts, and stratiform regions.

2) CALCULATION OF THE DISTANCE TO CONVECTIVE CORE

After determining the formation time and trajectory of the MCSs identified, the distance between the convective core and aircraft (L) was calculated. The method to determine L can be split into two steps. First, the coldest points of the MCS were identified by an algorithm. However, there could be many coldest points in different areas of a single MCS because a MCS can have multiple cores. In this case, the nearest and coldest point was defined as the convective core and used to calculate L. By analyzing the distributions of L and comparing with estimated L through scale on a map visually, the uncertainty of calculated L by algorithm is about 50 km in this study. Figure 1 shows an MCS identified at 1115:00 UTC 15 May 2015, with the magenta triangle representing the location of aircraft and the cyan asterisk with $BT_{10.8\mu m}$ of 213.6 K, denoting the convective core of the MCS. Following Chopde and Nichat (2013), the distance between the convective core and aircraft (L) was calculated as

$$L = 2(R+H)\sin^{-1} \times \sqrt{\sin^2\left(\frac{\phi_2-\phi_1}{2}\right) + \cos(\phi_1)\cos(\phi_2)\sin^2\left(\frac{\theta_2-\theta_1}{2}\right)}, \quad (3)$$

where R is the radius of Earth assumed to be 6371 km, H is the height of aircraft above the sea level, and ϕ_2 and ϕ_1 represent the longitude of the convective core and aircraft, respectively. θ_2 and θ_1 are the latitude of the convective core and aircraft, respectively. The temporal resolution of the *GOES-13* data are 30 min whereas the aircraft data are averaged to 5-s resolution. The in situ data are matched to the *GOES-13* data corresponding to the closest time so that the maximum time offset is 15 min. A total of 12 339 data points representing about 17.1 h of data in different environmental conditions within organized MCSs as summarized in Table 2.

3) $BTD_{6.8-10.8\mu m}$

Images of the infrared window at 10.8 μm are commonly used to derive motion vectors of cloudy areas in the troposphere (Nieman et al. 1997). Images of the water vapor channel at 6.7 μm are also used to determine upper troposphere motions in both cloudy and cloud-free environments (Velden et al. 1997). $BTD_{6.8-10.8\mu m}$ can be used to identify deep convective clouds because it takes large negative values for low-level clouds and its magnitude (absolute value) often decreases with rising cloud-top height, tending to zero near the tropopause (Donovan et al. 2008). By analyzing satellite observations and radiative transfer simulations, previous studies have found that $BTD_{6.8-10.8\mu m}$ can be positive when convective clouds penetrate the tropopause (Fritz and Laszlo 1993; Ackerman 1996; Levizzani and Setvák 1996; Wu et al. 2016), so the value of $BTD_{6.8-10.8\mu m}$ can represent the strength of convection. The

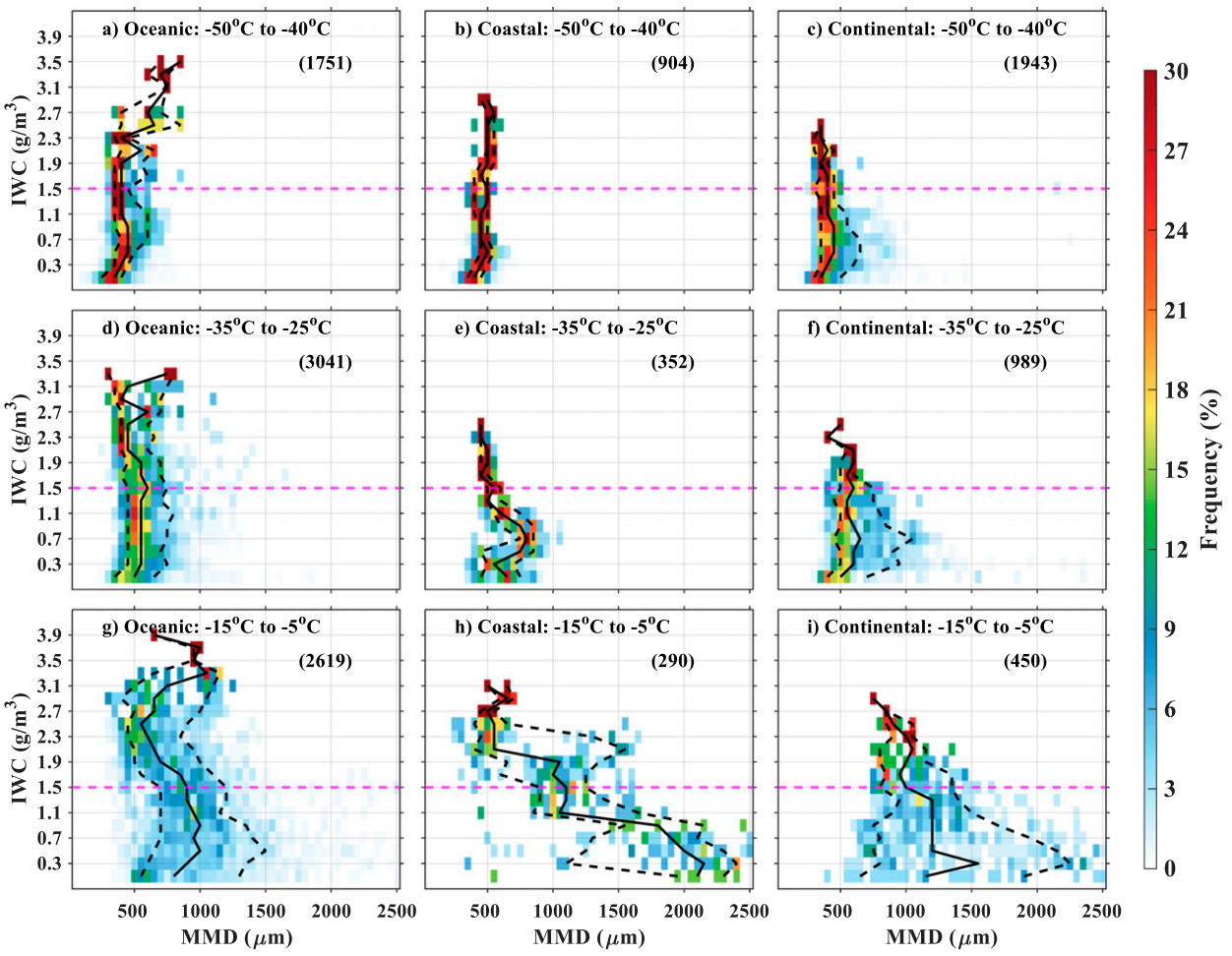

FIG. 7. As in Fig. 4, but for MCSs over different surfaces (oceanic, coastal, and continental) rather than for updrafts, downdrafts, and stratiform regions.

strength of convection can vary for different regions even in the same convective system, and microphysical processes may vary with local convective strength. Muhlbauer et al. (2014) investigated the relationship between cirrus microphysics and large-scale meteorology, finding that almost half of the cirrus cloud occurrences during the Department of Energy Small Particles in Cirrus (SPARTICUS) field campaign occurred in three distinct synoptic conditions, namely, upper-level ridges, mid-latitude cyclones with frontal systems, and subtropical flows. The strength of convection varied for these systems. Thus, the value of $BTD_{6.8–10.8\mu m}$ at the aircraft location was used as a measured of the local convection intensity, and to investigate the effect of convective intensity on ice crystal properties.

d. Classification of meteorological conditions

To understand controls of the ice crystal properties in MCSs (IWC, N_t, and MMD) and to identify when HIWC conditions occur, each measurement was classified according to several different meteorological conditions as follows: 1) The temperature (T) was divided into three levels ($-15° \le T \le -5°C$; $-35° \le T \le -25°C$; $-50° \le T \le -40°C$) with most of the data concentrated on the temperatures of the constant altitude legs of $-10°$, $-30°$, and $-45°C$; 2) Three kinds of cloud vertical motions, updrafts, downdrafts, and stratiform regions, were considered. A convective updraft was defined as any 5-s period when $w > 1\,m\,s^{-1}$ was sustained for at least four consecutive seconds, and a downdraft was defined as any 5-s period when $w < -1\,m\,s^{-1}$ was sustained for at least four consecutive seconds (Jorgensen et al. 1985; McFarquhar and Black 2004; Murphy et al. 2017). A stratiform (i.e., $-1 \le w \le 1\,m\,s^{-1}$) region was a period that had neither an updraft nor a downdraft present at the time of the observations. 3) The MCSs were separated into three groups according to whether the convection was over the ocean, coastline, or land (oceanic, coastal, and continental MCS). 4) The distance between the aircraft and the convective core of MCS (L) determined whether the observations were collected near the convective core or at the edge of the convective system ($L \le 50\,km$, $50 < L \le 100\,km$, $100 < L \le 200\,km$, $L > 200\,km$). 5) The MCS age was sorted into three groups (<6, 6–12, >12 h) to investigate observations at different stages of MCS. 6) The brightness temperature difference ($BTD_{6.8–10.8\mu m}$), which gives a measure of the

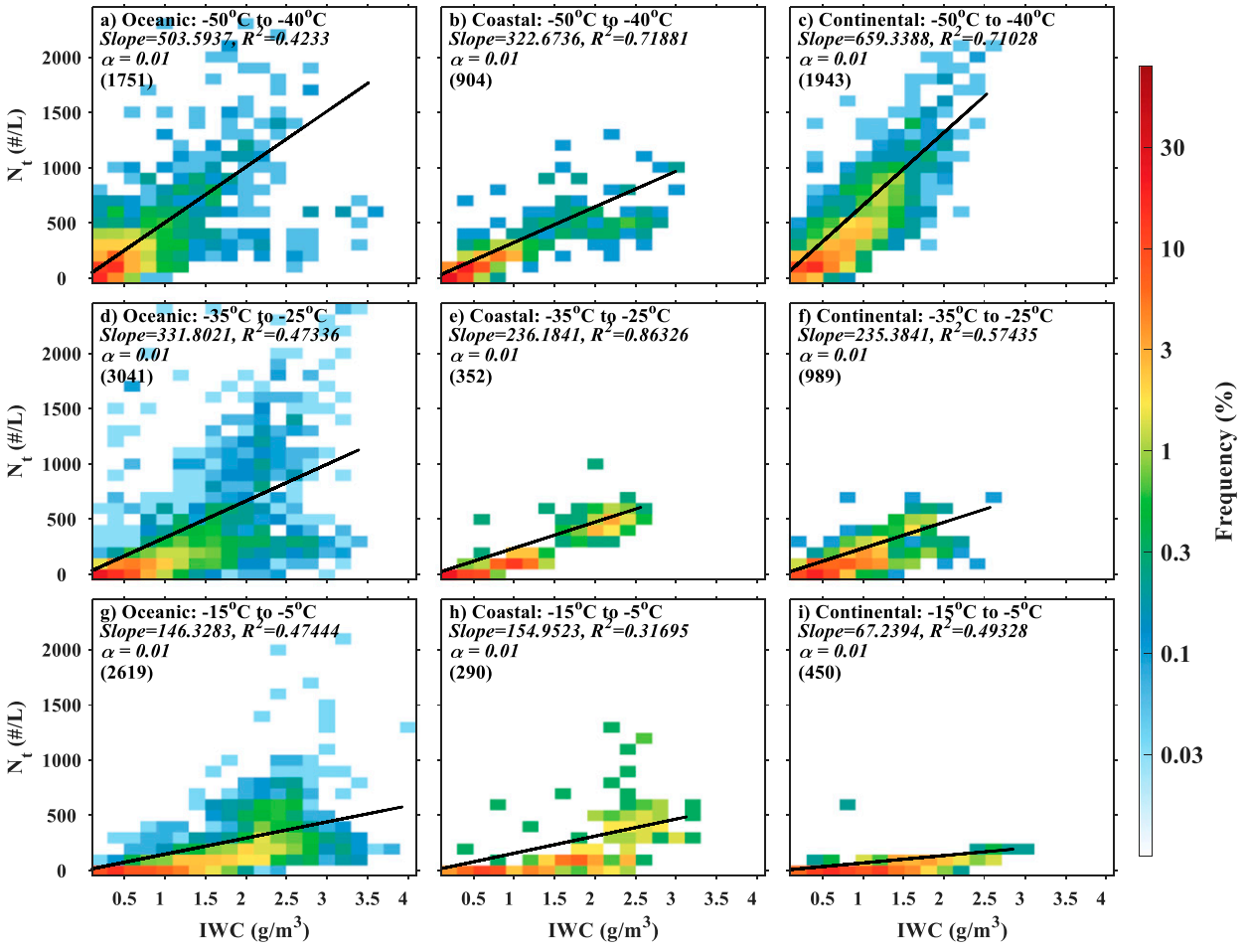

FIG. 8. As in Fig. 5, but for MCSs over different surfaces (oceanic, coastal, and continental) rather than for updrafts, downdrafts, and stratiform regions.

strength of local convection (Levizzani and Setvák 1996; Wu et al. 2016), was divided into three groups ($BTD_{6.8–10.8\mu m} < -3$ K, -3 to -1 K, > -1 K). Different criteria for segregating according to L (e.g., intervals: 25, 100, and 200 km), MCS age (e.g., intervals: 3 and 5 h), and $BTD_{6.8–10.8\mu m}$ (e.g., intervals: 2, 3, and 5 K) were tested, and the results showed that variation of classification threshold had little effect on the conclusions reached on how the properties varied with environmental conditions. Table 2 lists the number of 5-s samples that are available for each of these environmental conditions.

3. Case study: 15 May 2015

Figure 2 shows a time series of the microphysical properties measured by probes on the French Falcon 20 between 0924:44 and 1136:59 UTC 15 May 2015 during F13. The Falcon 20 flew at three constant temperature levels within the organized MCS as shown in the top panel (Fig. 2a), along with the distance between the aircraft and the convective core. Times segments when the Rosemount icing detector frequency was decreasing and was lower than 40 kHz and N_t measured by the CDP-2 was larger than 10 cm^{-3} are shaded by gray and cyan, respectively, and represent data assumed to be collected in clouds with liquid present. The LWC frequency was 0.64% for this event. This analysis focuses on three time periods. Period 1, marked by the black rectangle between 0929:39 and 0945:29 UTC in Fig. 2c, shows a negative correlation coefficient of -0.76 (Pearson method, p value: 10^{-36}) between IWC and MMD, with MMD between 400 and 800 μm when IWC > 1.5 g m^{-3}. The decrease of MMD with increasing IWC is consistent with the majority of cases during the Darwin campaign (Leroy et al. 2017), and shows these HIWC regions are mainly associated with small particles. On the other hand, MMD reached about 2000 μm when IWC decreases to 0.5 g m^{-3} at around 0943 UTC. Another period of HIWC was sampled at a lower temperature level from $-50° \le T \le -40$°C. This HIWC event corresponds to measurements near the convective core as shown in period 2 marked by a blue rectangle between 1101:04 and 1111:04 UTC. This period is illustrated by the blue points that represent data with IWC > 1.5 g m^{-3} and MMD < 400 μm (Fig. 1). These data were obtained in a region with $BT_{10.8\mu m} <$ 235 K, which was near the peak of convection (marked by a cyan asterisk with $BT_{10.8\mu m} = 213.6$ K), showing that processes within the convective core of this MCS were favorable for the

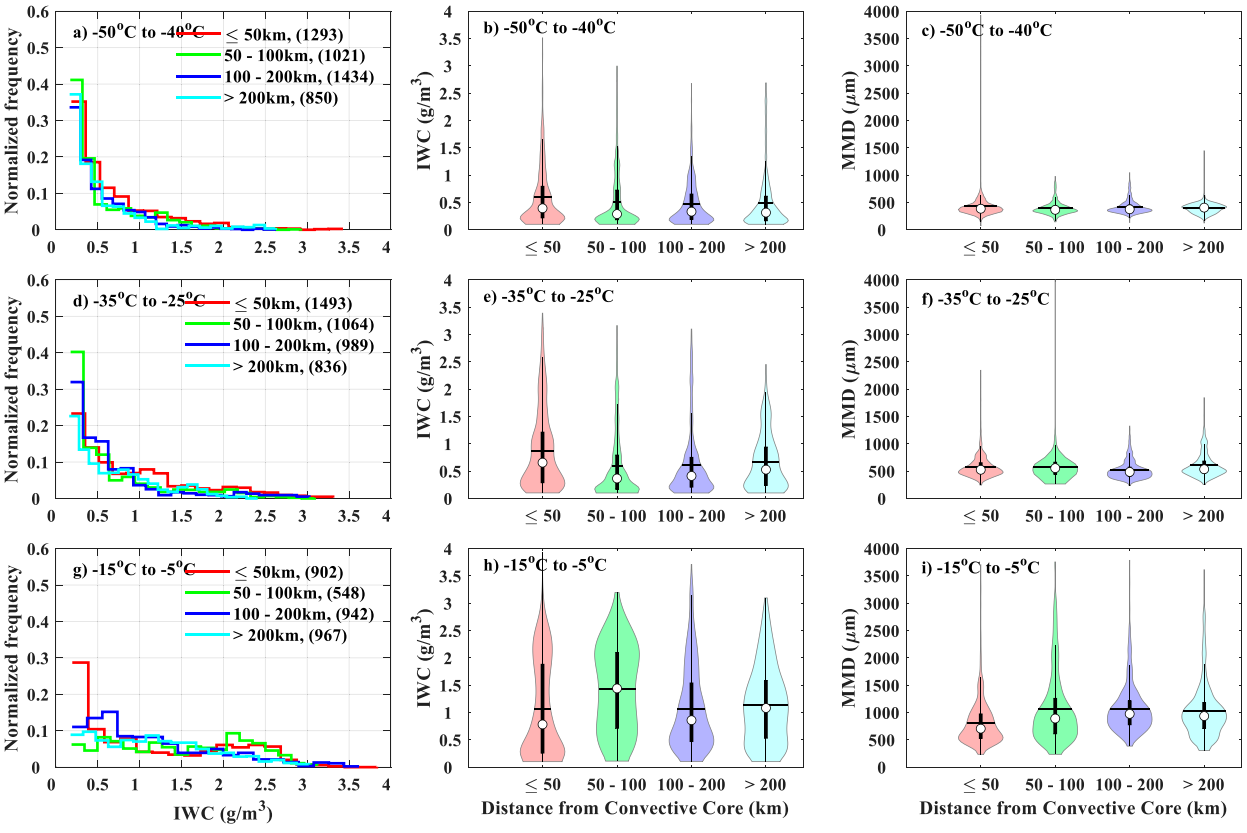

FIG. 9. As in Fig. 3, but for MCSs sorted by distance of measurement from convective core ($L \leq 50$ km, $50 < L \leq 100$ km, $100 < L \leq 200$ km, $L > 200$ km) rather than for updrafts, downdrafts, and stratiform regions.

generation of HIWC with small ice crystals. There are also time periods when small MMD occur in a region with IWC $< 0.5\,\mathrm{g\,m^{-3}}$ as seen in period 3 marked by the green rectangle between 1118:04 and 1126:04 UTC in Fig. 2c. This region exhibits a weak positive correlation coefficient of 0.29 (Pearson method, p value: 0.016) between IWC and MMD, and shows that MMD can reach around 400 μm even when IWC $< 0.5\,\mathrm{g\,m^{-3}}$. In general, for the times with HIWCs, there are large N_t (Fig. 2g), indicating a positive correlation between IWC and N_t. However, the relationship between N_t and IWC varies for different T. The HIWC regions typically occur for large updrafts and downdrafts as displayed in Fig. 2d, similar to simulation results of Franklin et al. (2016) and Stanford et al. (2017), and to the observations of McFarquhar and Black (2004) and Mascio et al. (2020) that showed the PSD shape was influenced by w.

To summarize the findings from this case, the correlation between IWC and MMD was negative in the region with IWC $> 1.5\,\mathrm{g\,m^{-3}}$, whereas there was a positive correlation when IWC $< 0.5\,\mathrm{g\,m^{-3}}$. The convective core of the MCS was favorable for the generation of HIWC regions with small ice crystals. Other case studies were examined and showed similar results.

4. Statistical analysis on controls of HIWC regions

To better investigate where HIWC regions are likely to occur and to better investigate how environmental conditions control the microphysical properties of these regions, a statistical analysis of all data (12 339 points, ~17.1 h) obtained by Falcon 20 during the Cayenne campaign was conducted. The conditions sampled during the 17 flights of the Cayenne HAIC-HIWC campaign are summarized in Table 1, including information on the IWC measured by IKP2 as a function of the temperature at flight level, the underlying surface conditions, and the initial and dissipation times of the MCS sampled. The data are separated into different groups according to temperature, vertical motion, underlying surface, distance away from the convective core, system age, and $\mathrm{BTD}_{6.8\text{–}10.8\mu\mathrm{m}}$ as discussed in section 2. Table 2 shows the number of 5-s measurements that were obtained under each of these conditions.

a. *Vertical velocity*

In this section, distributions of IWC, MMD and N_t for different vertical motions (i.e., convective updrafts, downdrafts, and stratiform regions) are compared. Figures 3a, 3d, and 3g show the normalized frequency of occurrence of IWC for the three vertical motions as a function of T. The fractional frequency of occurrence of HIWC conditions, namely times when IWC $> 1.5\,\mathrm{g\,m^{-3}}$, is greater for updrafts than for downdrafts and stratiform regions. The frequency of HIWC points also decreases with decreasing T, with almost all (96.4%) IWCs measured in stratiform regions at $-50° \leq T \leq -40°$C less than $1.5\,\mathrm{g\,m^{-3}}$. Figures 3b, 3e, and 3h show the minimum, 5th, 25th,

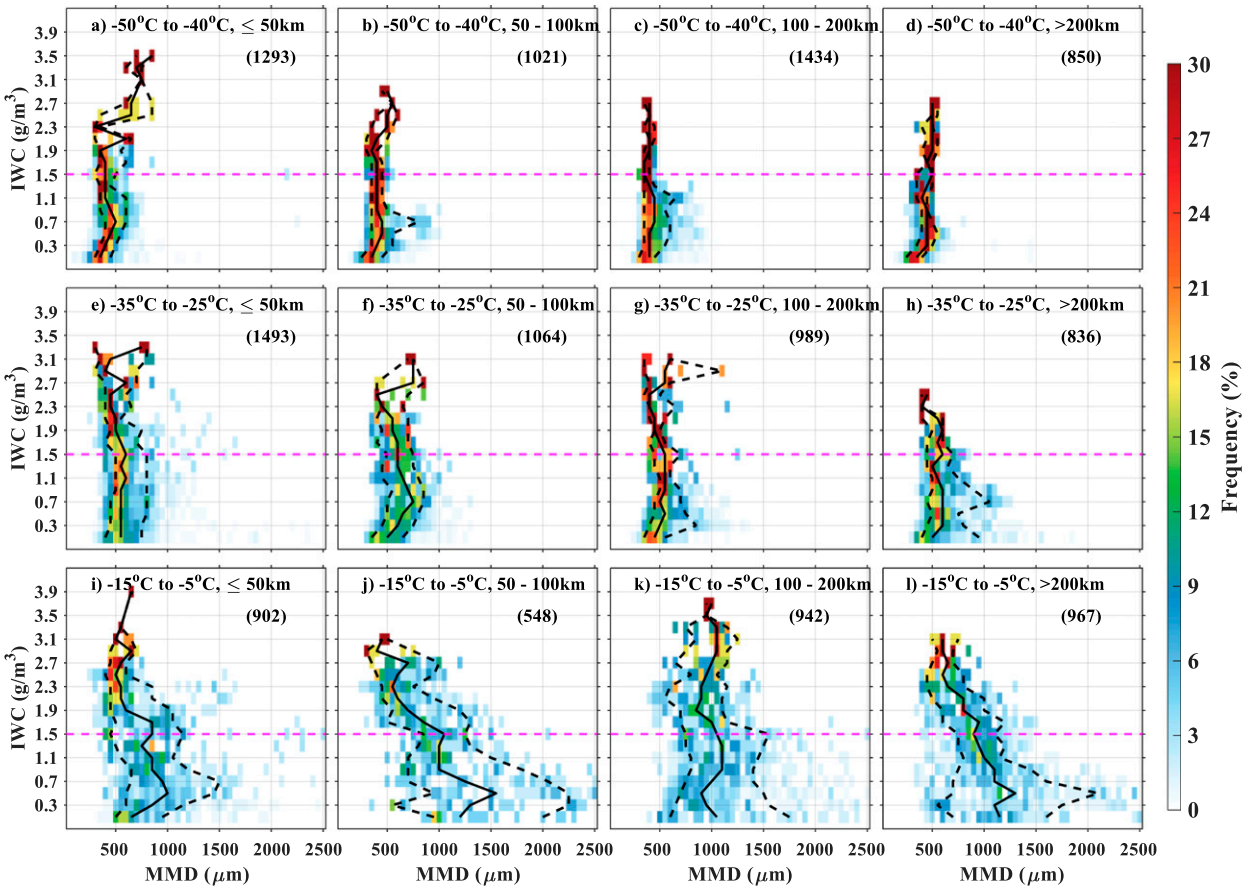

FIG. 10. As in Fig. 4, but for MCSs sorted by distance of measurement from convective core ($L \leq 50$ km, $50 < L \leq 100$ km, $100 < L \leq 200$ km, $L > 200$ km) rather than for updrafts, downdrafts, and stratiform regions.

50th, 75th, 95th, maximum, and mean IWCs for data obtained within the three vertical motions for different T. The violin plots give further information about the distribution of parameters. These plots again show that the IWC obtained in updrafts is larger than in downdrafts or stratiform regions. Almost 95% of IWCs obtained in updrafts are larger than 1.0 g m^{-3} for $-15° \leq T \leq -5$°C, with the mean IWC larger than 1.0 g m^{-3} for all three T. Inferences about the physical processes occurring in the convection can be made from these findings. For example, this shows that the convective updrafts are the main source of the high IWCs. The IWCs in the stratiform regions are smaller than in updrafts or downdrafts. The MMD for the three cloud types shown in Figs. 3c, 3f, and 3i show that the MMD in updrafts are smaller than those in downdrafts and stratiform regions for $T \geq -15$°C. The fact that the IWCs are very large in updrafts means that a lot of small ice crystals must be present in the updrafts and thus are being generated there by heterogeneous nucleation. On the other hand, there is no significant difference in MMD for the three vertical motions when $T \leq -25$°C, with the difference in MMD between downdrafts and stratiform regions not passing the 5% significance level (figures not shown).

The normalized frequency of MMD for each IWC range for convective updrafts, downdrafts and stratiform regions is shown in Fig. 4. The majority of MMD range from 400 to 1800 μm for $-15° \leq T \leq -5$°C (Fig. 4l), 200 to 800 μm for $-35° \leq T \leq -25$°C (Fig. 4h), and 150 to 600 μm for $-50° \leq T \leq -40$°C (Fig. 4d). The ranges of MMD decrease sharply with decreasing T, consistent with the results of Leroy et al. (2016a) for the Cayenne campaign. The increase of MMD with increasing T is consistent with growth by aggregation and sedimentation of larger particles to lower altitudes. Further, the analysis is consistent with the sublimation of small ice crystals in subsaturated environments, keeping the concentration of ice crystals with $D_{max} < 100$ μm relatively low (Korolev et al. 2011, 2013b). The MMD increased with IWC when IWC < 0.5 g m^{-3} and IWC > 2.4 g m^{-3} at all three T, consistent with period 3 shown in Fig. 2. However, the MMD decreased sharply with IWC for 0.5 $<$ IWC ≤ 2.4 g m^{-3} at $-15° \leq T \leq -5$°C (Fig. 4l) and slightly when $T < -15$°C. In general, IWC was positively correlated with MMD for stratiform regions when IWC < 0.5 g m^{-3}. In the convective updrafts the mean MMD of the updraft regions stayed around 500 μm for all three T, probably because the convective environment is more favorable for the generation of small ice crystals through heterogeneous or homogeneous nucleation. Further, particle collisions are more frequent given the higher N_t, suggesting many small ice crystals could be produced by

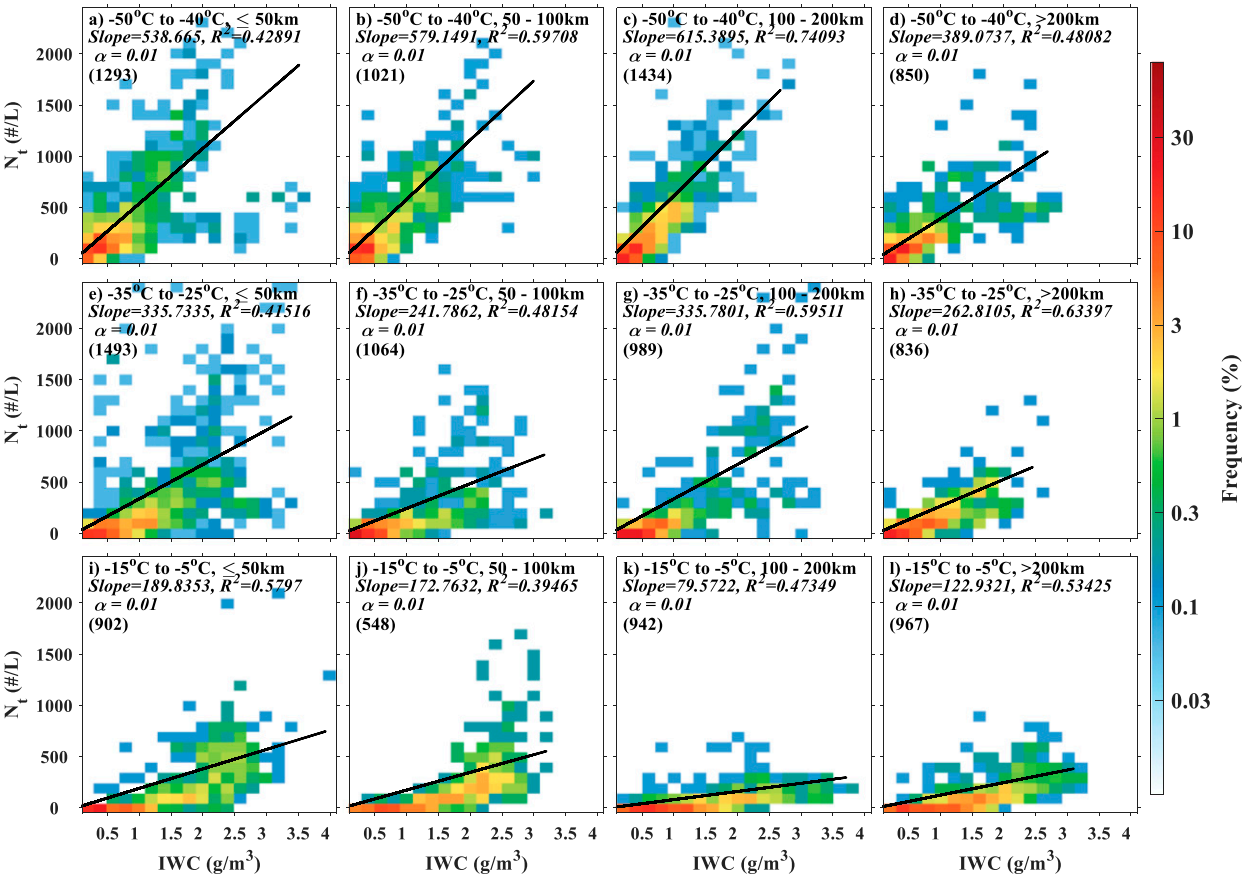

FIG. 11. As in Fig. 5, but for MCSs sorted by distance from convective core ($L \leq 50$ km, $50 < L \leq 100$ km, $100 < L \leq 200$ km, $L > 200$ km) rather than for updrafts, downdrafts, and stratiform regions.

secondary ice production processes (Korolev et al. 2020), perhaps for time periods when large supercooled drops are present.

Normalized two-dimensional frequency distributions of N_t and IWC for updrafts, downdrafts and stratiform regions are shown in Fig. 5. The relative uncertainty of N_t is typically around 50% and the maximum value N_t is about 2000 L^{-1} in this study. This value is smaller than the N_t reported by Fontaine et al. (2017), who found that most N_t for ice crystal diameters between 15 and 12 845 μm are less than 10^4 L^{-1} and sometimes on the order of 10^5 L^{-1} for data obtained from the Darwin HAIC/HIWC field campaign. The differences occur because Fontaine et al. (2017) included the concentrations of small crystals (<55 μm) in the calculation of N_t, but the current study does not because particles in this size range have large but highly uncertain concentrations due to a small and poorly defined depth of field for such small particles (Korolev et al. 1998). The slope of the best fit line between IWC and N_t and R^2 increases with decreasing T. The N_t at the lower T are always larger than those at a higher T for the same IWC, meaning the relationship between N_t and T is negative. This is similar to the findings of Heymsfield et al. (2013) who noted the trend was a result of ice aggregation at lower altitude, and consistent with an increase of activity of ice nucleating particles with decreasing T (e.g., Fletcher 2011; Cooper 1986; Meyers et al. 1992; DeMott et al. 2010). On the other hand, Krämer et al. (2009) found a positive correlation between N_t and T. The N_t increase with IWC when IWC < 2.4 g m^{-3}, and decrease with IWC when IWC > 2.4 g m^{-3} at $-15° \leq T \leq -5°$C, is consistent with Fig. 4l and the presence of abundant small crystals in HIWC conditions. For the same IWC, N_t (updraft) > N_t (downdraft) > N_t (stratiform) when $T > -35°$C, with a similar slope for $-50° \leq T \leq -40°$C. In general, there are significant differences between the updrafts and the other two regions, and less substantial differences between downdrafts and stratiform regions (figures not shown).

b. Surface characteristics beneath MCSs

Similar tests were conducted to determine whether the surfaces over which the aircraft flew were correlated with the microphysical distributions. The MCSs were divided into oceanic, coastal, and continental MCSs according to the underlying surface over which the flights occurred regardless of where the MCS originally formed. Figure 6 shows that IWCs in oceanic and coastal convective systems were usually greater than those in continental systems when $-15° \leq T \leq -5°$C, as for example, 66.2% of points within coastal MCSs had IWCs larger than 1.0 g m^{-3}. But, IWCs in continental MCSs were

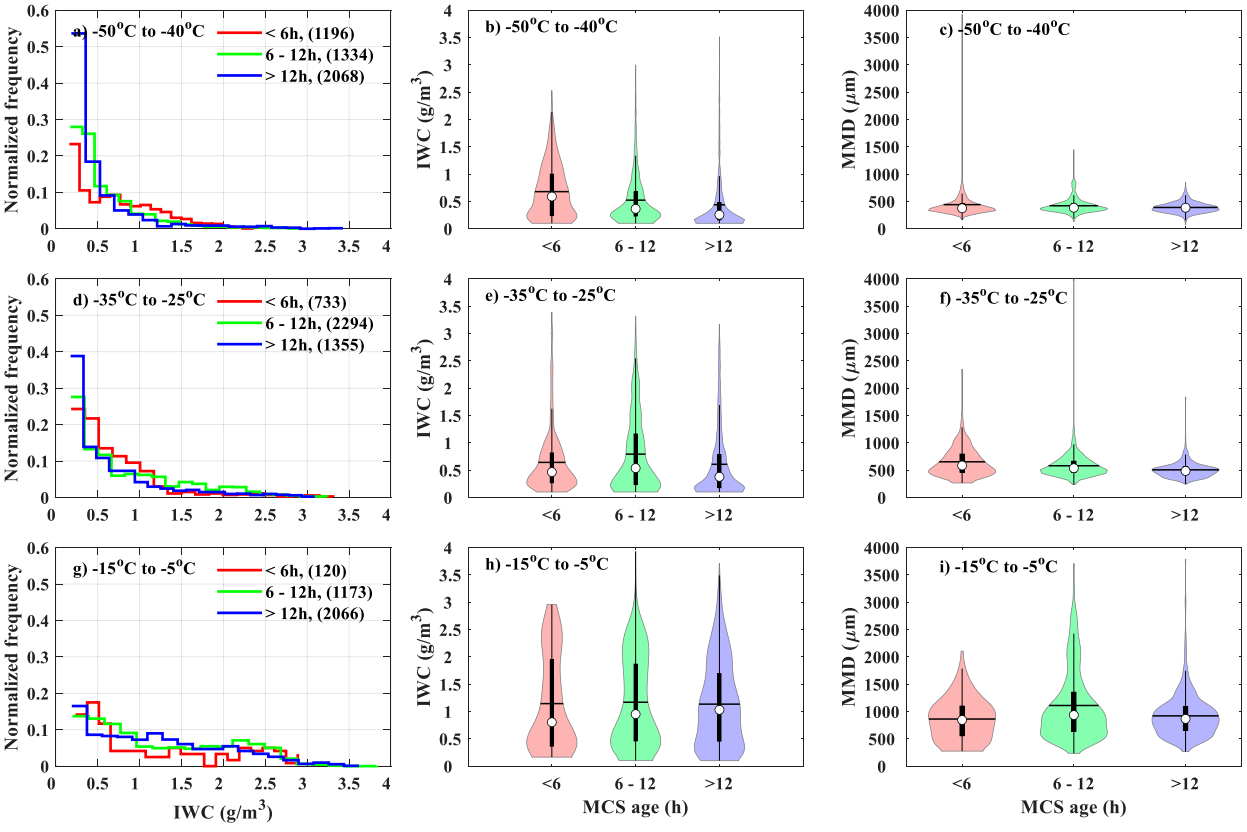

FIG. 12. As in Fig. 3, but for MCSs sorted by age (<6, 6–12, and >12 h) rather than for updrafts, downdrafts, and stratiform regions.

greater than for the other two surface characteristics at $-50° \leq T \leq -40°C$. The mean MMD in continental MCSs is the greatest, while the MMD in oceanic MCSs is the smallest at $-15° \leq T \leq -5°C$. The two-sample Kolmogorov–Smirnov test method with a 5% significance level was applied in this study and there is not a significant difference in MMD when $T \leq -25°C$ for the different surface types. But, in general, the mean MMD decreases with decreasing T for the three surface conditions beneath MCSs. Figure 7 shows the normalized frequency of MMD for each IWC range for the different surfaces at three T. The MMD increase with IWC from 0.1 to 0.5 g m^{-3} for oceanic and continental MCSs when $-15° \leq T \leq -5°C$, but decrease sharply with IWC at the same T for coastal MCSs. MMD all increase with IWC from 0.1 to 0.5 g m^{-3} for three kinds of MCSs when $T \leq -25°C$.

Normalized two-dimensional frequency distributions of N_t and IWC for the three types of surfaces are shown in Fig. 8. The slopes of the best fit lines all increase with decreasing T. For the same IWC, N_t (oceanic) > N_t (coastal) > N_t (continental) when $T \geq -35°C$, while N_t (coastal) < N_t (oceanic) < N_t (continental) when $-50° \leq T \leq -40°C$. The value of N_t does not change with IWC in a statistically significant fashion for continental systems when $-15° \leq T \leq -5°C$. The slope of the fit line for the continental MCSs changes most with decreasing T, with the positive correlation between N_t and IWC becoming particularly significant (significance level $\alpha = 0.01$) at $-50° \leq T \leq -40°C$. This means more small ice crystals are found in continental MCSs at the lower temperature levels, consistent with the convective available potential energy (CAPE) being greater over the mainland (~1386.4 J kg^{-1}) than over the ocean (~927.3 J kg^{-1}). The greater number of small crystals at the higher temperatures in the oceanic systems may be associated with the fact that convection is typically weaker over the oceans than over the continents (e.g., Lucas et al. 1994; Zipser et al. 2006; Matsui et al. 2016) so that they are not transported as far upward. Differences in storm intensity and proximity to the convective core could have minimized the differences of distributions of IWC and MMD with respect to the variation with surface type (e.g., continent and ocean).

c. *Distances away from the convective core*

Lawson et al. (2010) found that IWCs in tropical anvil cirrus decrease with increasing distance away from the convection. Yost et al. (2018) also found that IWCs decrease as the distance away from overshooting tops increases. McFarquhar and Heymsfield (1996) found similar trends for three oceanic MCSs sampled. However, most of these studies were limited to distances approximately 100 km away from convective cores. In this section, the dependence of the microphysical properties with distance from the convective core as a function of T is analyzed by categorizing the data according to the distance between the aircraft and convective core, L, into four

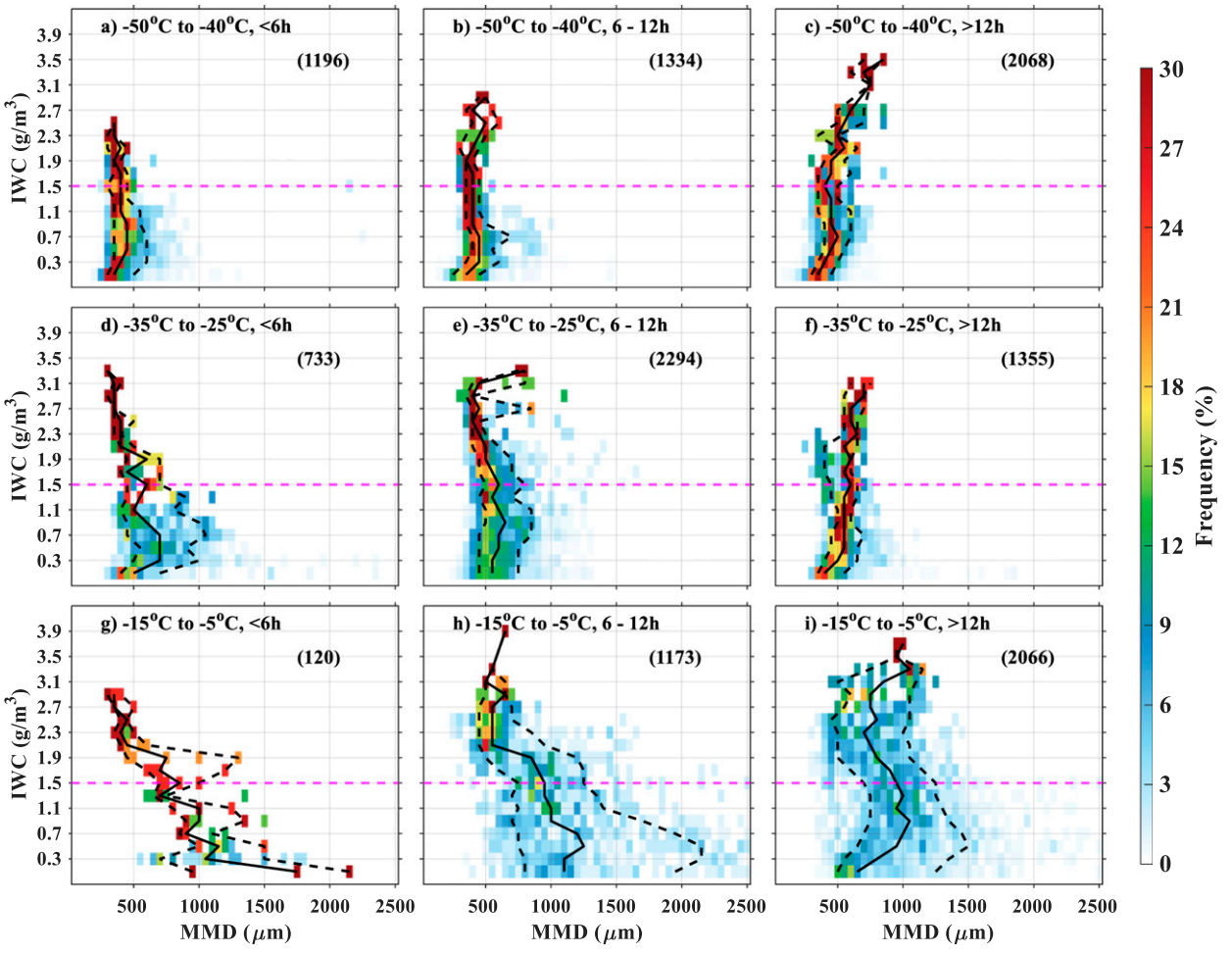

FIG. 13. As in Fig. 4, but for MCSs sorted by age (<6, 6–12, and >12 h) rather than for updrafts, downdrafts, and stratiform regions.

groups: $L \le 50$ km, $50 < L \le 100$ km, $100 < L \le 200$ km, and $L > 200$ km.

The mean IWC decreases with increasing L at $-50° \le T \le -40°$C in Fig. 9b, consistent with the analysis of period 2 in Fig. 2. But different trends can be noted at the higher T, similar to the analysis of IWCs shown in Korolev et al. (2018). These results emphasize that the level must be accounted for when analyzing trends of IWC with L, something that was not accounted for in some previous studies. The MMD near the convective core are smaller than those further from the convective core at $-15° \le T \le -5°$C, with a less significant difference when $T \le -25°$C. Figure 10 shows the normalized frequency of MMD for each IWC range for different L at three T. At $-15° \le T \le -5°$C, the MMD increase with increasing IWC from 0.1 to 0.5 g m^{-3}, and then decrease with increasing IWC when IWC > 0.5 g m^{-3} for the regions with $L \le 100$ km and $L > 200$ km. However, the median MMD for $100 < L \le 200$ km stays between 800 and 1200 μm even when larger changes of IWC are noted. Thus, at $-15° \le T \le -5°$C, the MMD obtained for $100 < L \le 200$ km are greater than for the other three regions for the same IWC when IWC > 0.5 g m^{-3}, perhaps because the environmental conditions within this region favor aggregation and sedimentation. In addition, as L increases the small-scale dynamical activity in the ice clouds (e.g., Lilly 1988) will play an increasingly important role in determining both IWC and MMD so that their distributions are less tied to the properties of the convection. Overall, IWC measured near the convective core is greater than those regions away from the convective core, due to spreading of the anvil, sublimation or aggregation of the smaller particles, and sedimentation of the larger particles.

Normalized two-dimensional frequency distributions of N_t and IWC under different L are shown in Fig. 11. The slopes of the fit lines increase with decreasing T for different L. The slope of the fit line is the smallest (79.6 g^{-1} m^3 L^{-1}) for $100 < L \le 200$ km at $-15° \le T \le -5°$C, corresponding to the median of MMD staying around 1000 μm even when IWCs change as shown in Fig. 10k. This may mean ice crystals experience aggregation and sedimentation in this region to a greater extent than compared to other L regions at $-15° \le T \le -5°$C, or alternatively, in situ growth mechanisms due to internal dynamics may also be of importance. The role of ice particles generated in the convective core being transported and falling

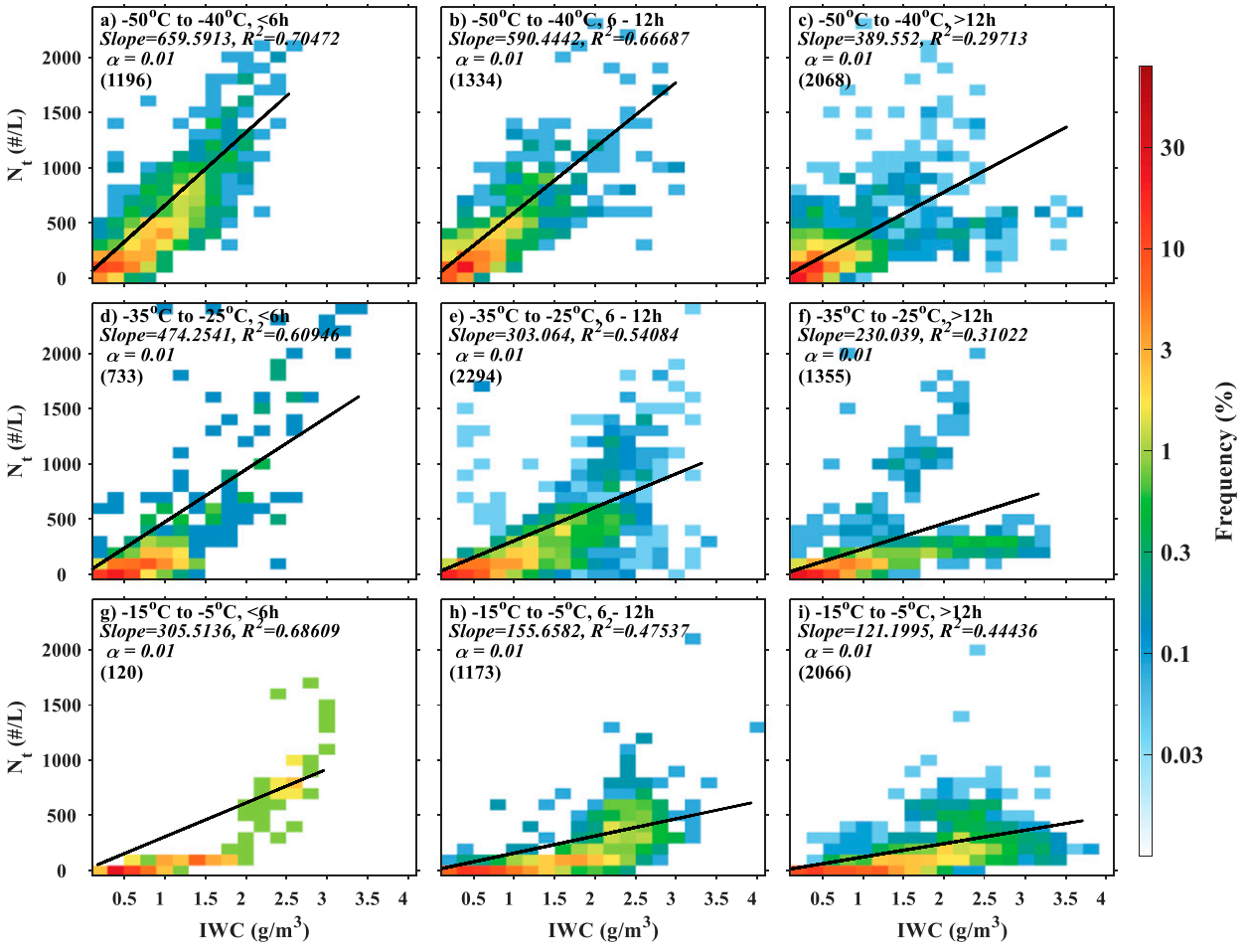

FIG. 14. As in Fig. 5, but for MCSs sorted by age (<6, 6–12, and >12 h) rather than for updrafts, downdrafts, and stratiform regions.

into this region because of advection of particles caused by horizontal wind effect must also be taken into account.

d. MCS age

Lawson et al. (2010) found that IWCs in tropical anvil cirrus decrease with the age of the anvil. The impact of the MCS age on the distributions of IWCs and MMD is shown in Fig. 12. The IWC in the 6–12 h age is usually greater than in the <6 h and >12 h age when $T > -35$°C. This is consistent with the 6–12 h stage being in the developing or mature stage after ice has started being injected into the anvil (Leary and Houze 1980), with many ice crystals being created and growing by aggregation. It is also noted that IWCs decrease with the increasing system age at $-50° \le T \le -40$°C most likely because the crystals are falling out from the higher levels of the anvil. The IWC in the >12 h age is the smallest, consistent with sublimation and a weakening and dissipation of MCSs not being conducive to the generation and growth of ice particles. The scatter in the data is no doubt associated with variations in the location of the measurements, variations in the intensity of the convection, and likely varying amounts of growth due to small-scale motions in the MCS. The mean MMD with <6 h age is smaller than those with MCS age >6 h when $-15° \le T \le -5$°C, with no significant difference of MMD with MCS age shown at $T \le -25$°C. The smaller MMD for young MCSs is consistent with the generation of new particles that have not experienced appreciable growth with deposition, accretion, or aggregation. Figure 13 shows the normalized frequency of MMD for each IWC range for different MCS ages at three T. The relationship between IWC and MMD is positive for MCS age > 6 h when IWC $< 0.5\,\mathrm{g\,m^{-3}}$ at $-15° \le T \le -5$°C, while the MMD decrease continually with IWC from about 1600 to 400 μm for MCSs age <6 h at the same T. This is consistent with HIWC regions in the younger MCSs being dominated by small ice crystals nucleated within the active convection and subsequently being injected into the anvil. It is also noted that MMD for >12 h age is larger than age <12 h for the same IWC when IWC $> 0.5\,\mathrm{g\,m^{-3}}$ at $-15° \le T \le -5$°C.

Figure 14 shows normalized two-dimensional frequency distributions of N_t and IWC as a function of MCS age. The slopes of the fit lines increase with decreasing T for different ages, especially it can increase from $155.7\,\mathrm{g^{-1}\,m^3\,L^{-1}}$ at $-15° \le T \le -5$°C to $590.4\,\mathrm{g^{-1}\,m^3\,L^{-1}}$ at $-50° \le T \le -40$°C in the MCS age with 6–12 h. While the linear relationship does not

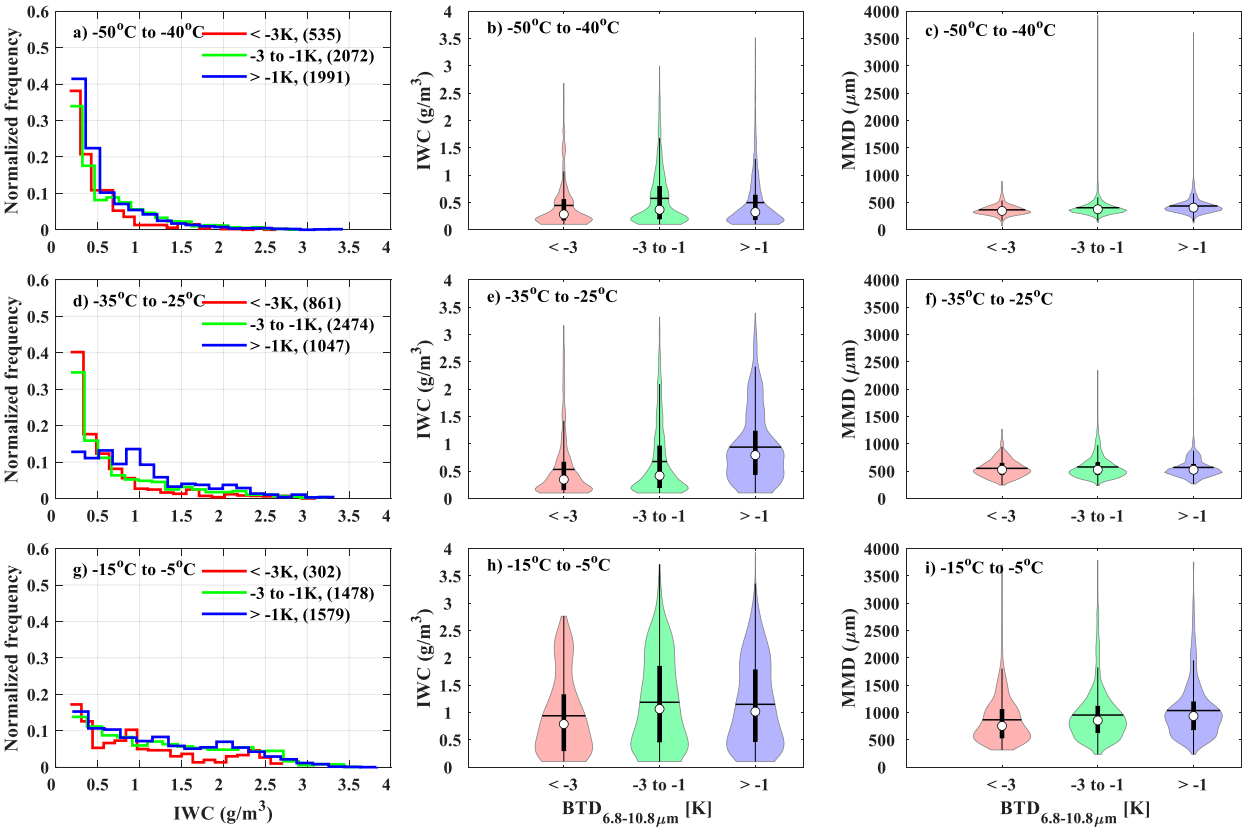

FIG. 15. As in Fig. 3, but for MCSs sorted by $BTD_{6.8–10.8\mu m}$ (< −3 K, −3 to −1 K, > −1 K) rather than for updrafts, downdrafts, and stratiform regions.

increase significantly with decreasing T for the MCS age >12 h, the distribution of frequency for MCS ages >12 h at $T \leq -25$°C shows two modes above and below the fit line, consistent with the weak positive relationship between IWC and MMD shown in Figs. 14c and 14f. Overall, for the same IWC, N_t among different MCSs ages shows that N_t (<6 h) > N_t (6–12 h) > N_t (>12 h) for three T, meaning more small ice crystals are found in younger convective systems for the same IWCs, with numbers decreasing as the system ages consistent with the action of aggregation or a smaller rate of injection of small crystals into the anvil from active convection. Small-scale dynamical activity in the anvil cloud obfuscates some of these trends.

e. *Effect of $BTD_{6.8–10.8\mu m}$*

The $BTD_{6.8–10.8\mu m}$ at the location of the aircraft can reflect the local strength of convection as detected by *GOES-13*. In this section, the $BTD_{6.8–10.8\mu m}$ were separated into three groups (< −3 K, −3 to −1 K, and > −1 K) at each T to investigate the effects of local convection strength on the microphysical properties. Figure 15 shows IWCs and MMD distributions for different $BTD_{6.8–10.8\mu m}$ at three T. The IWCs increase with increasing $BTD_{6.8–10.8\mu m}$ for three T, indicating stronger convection favors the generation of more mass of ice crystals. However, MMD shows no significant difference with $BTD_{6.8–10.8\mu m}$ at all three T. This could be associated with the lifting of large amounts of hydrometeors to a high altitude in regions of strong convection (Bouniol et al. 2016), with the nucleation of more particles there. Figure 16 shows the normalized frequency of MMD for each IWC range as a function of $BTD_{6.8–10.8\mu m}$ at three T. The trends of MMD with increasing IWC between different groups of $BTD_{6.8–10.8\mu m}$ are not significantly different, showing the strength of the convection does not seem to affect the size of the crystals generated.

Normalized two-dimensional frequency distributions of N_t and IWC for different $BTD_{6.8–10.8\,\mu m}$ are shown in Fig. 17. The slopes of the fit lines all increase with decreasing T for different $BTD_{6.8–10.8\,\mu m}$. For the same IWC, N_t among different groups of $BTD_{6.8–10.8\,\mu m}$ shows that N_t (< −3 K) > N_t (−3 to −1 K) > N_t (> −1 K) at $-50° \leq T \leq -40$°C, while the results are N_t (−3 to −1 K) > N_t (> −1 K) > N_t (< −3 K) at $-35° \leq T \leq -25$°C, and no statistically significant difference is noted for three groups at $-15° \leq T \leq -5$°C. Thus, there seem to be no clear trends on how the strength of the convection affects the sizes of the crystals.

5. Conclusions

The variation of distributions of microphysical parameters, such as ice water content (IWC), total number concentrations (N_t), and mass median diameter (MMD) with environmental conditions was examined using data obtained during the

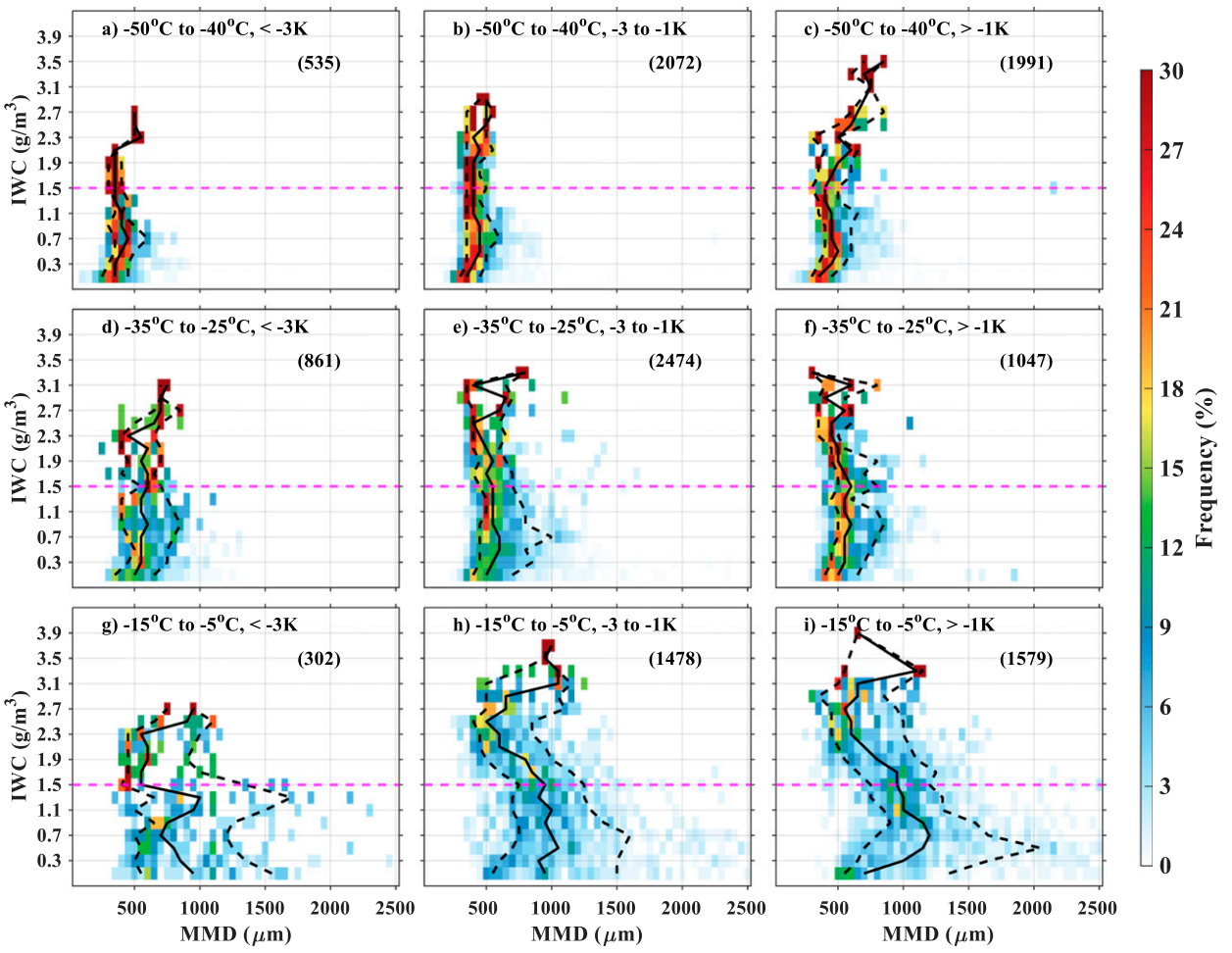

FIG. 16. As in Fig. 4, but for MCSs sorted by $BTD_{6.8–10.8\mu m}$ (< -3 K, -3 to -1 K, > -1 K) rather than for updrafts, downdrafts, and stratiform regions.

second HAIC-HIWC flight campaign conducted from 9 to 29 May 2015 out of Cayenne, French Guiana. Data were separated according to temperature (T, $-15° \le T \le -5°$C; $-35° \le T \le -25°$C; $-50° \le T \le -40°$C), vertical velocity (updrafts, downdrafts, and stratiform cloud regions), surface conditions (oceanic, coastal and continental), distance away from the convective core ($L \le 50$ km, $50 < L \le 100$ km, $100 < L \le 200$ km, $L > 200$ km), MCS age (<6 h, 6–12 h, >12 h), and convective strength ($BTD_{6.8–10.8\mu m} < -3$ K, -3 to -1 K, > -1 K). A paired test was used to test for statistically significant differences between distributions as functions of these environmental conditions. The difference of microphysical properties between the HIWC region was also contrasted against those obtained in regions without HIWCs. The principal findings of this study are as follows:

1) T has highest correlation with IWC and MMD. High IWCs are more likely to occur at higher T. MMD are mainly in the range of 400–1800 μm for $-15° \le T \le -5°$C, 200–800 μm for $-35° \le T \le -25°$C, and 150–600 μm for $-50° \le T \le -40°$C, showing a sharp decrease with decreasing T. The negative correlation between N_t and T noted is consistent with ice particle growth by vapor deposition and aggregation during descent in anvils.
2) At $-15° \le T \le -5°$C, MMD increase with increasing IWC when IWC < 0.5 g m^{-3}, decrease when 0.5 g m^{-3} < IWC < 2.4 g m^{-3}, and are the smallest for IWC > 2.4 g m^{-3} for most environmental conditions (e.g., updrafts and downdrafts, coastal and continental MCS, MCS age <12 h, and $BTD_{6.8–10.8\mu m} < -3$ K). This shows that the HIWC regions are dominated by small ice crystals. There are some regions with exceptions to these trends (e.g., MMD does not vary significantly with IWC for $100 \le L \le 200$ km, and MMD increases with IWC for system age >12 h when $T \le -25°$C). The strength of dependence of the relationship between IWC and MMD on environmental conditions decreases with decreasing T.
3) The distributions of IWC are statistically correlated with the strength of vertical velocity. HIWC regions usually occur for large upward w or downward w. IWC in updrafts is likely to be larger than in downdrafts and stratiform clouds at all T, meaning the convective environment is more favorable for the nucleation of small ice crystals.

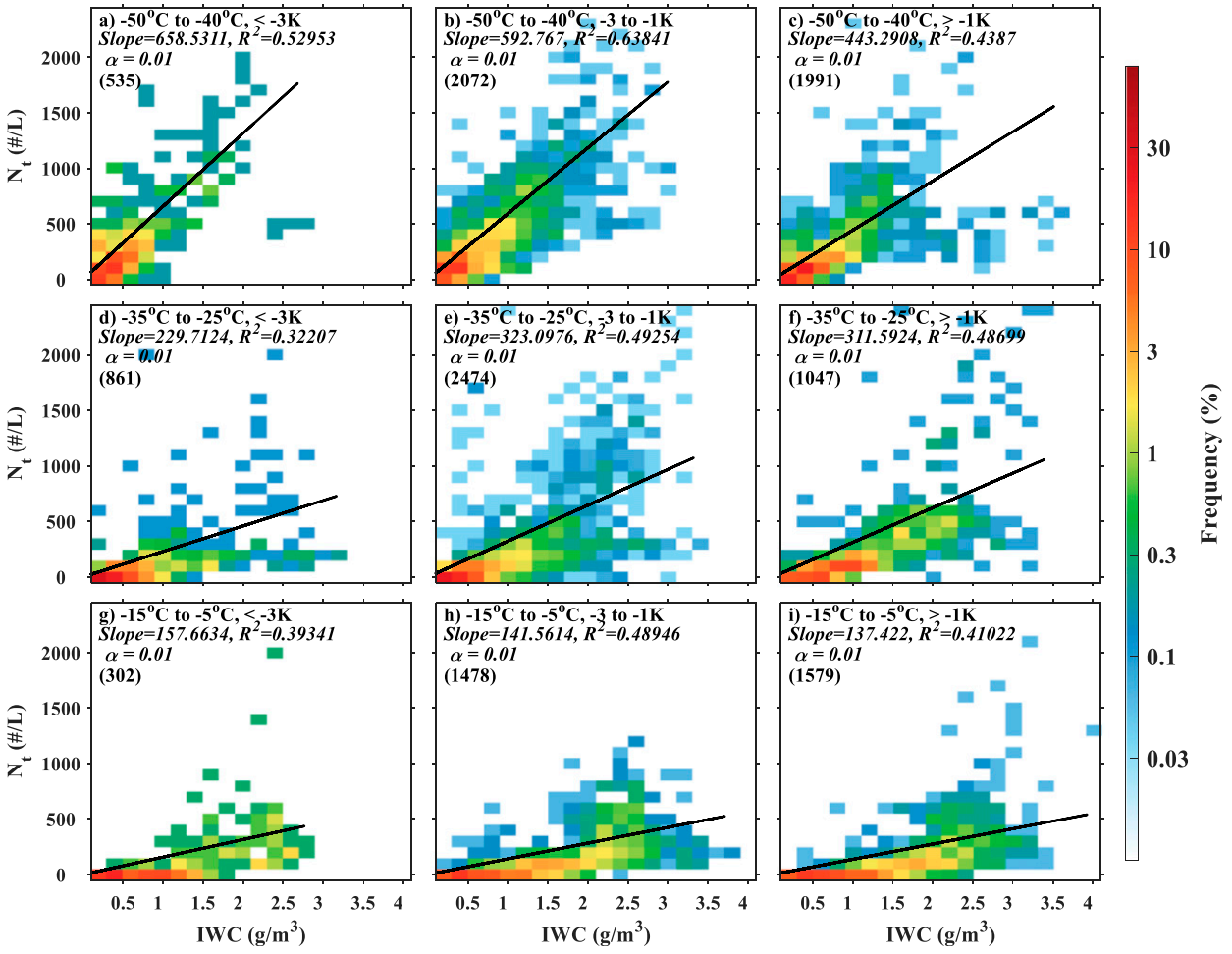

FIG. 17. As in Fig. 5, but for MCSs sorted by $BTD_{6.8–10.8\mu m}$ (< −3 K, −3 to −1 K, > −1 K) rather than for updrafts, downdrafts, and stratiform regions.

4) More small ice crystals are found in continental MCSs at lower T, consistent with the convection being more intense over the mainland.
5) IWCs for MCS ages between 6 and 12 h at higher T are the largest. Most MCSs with ages between 6 and 12 h are in the mature stage, and hence there is significant outflow of fresh particles to the surrounding regions. Ice crystals may experience more aggregation and deposition growth in older MCSs with less outflow, explaining why MMD are larger in older MCSs.
6) For $-50° \le T \le -40°C$, IWC is highly correlated to distance from the convective core, with IWC decreasing with increasing L. HIWC regions can exist around the convective core and the regions away from the convective core for $-15° \le T \le -5°C$, consistent with the analysis of Korolev et al. (2018).
7) IWCs increase with increasing $BTD_{6.8–10.8\mu m}$ at different T whereas MMD show no significant differences for different $BTD_{6.8–10.8\mu m}$, meaning the more intense convection generates more ice, but does not necessarily affect the sizes of the particles generated.
8) The strength of correlations between N_t and IWC all increases with decreasing T for different environmental conditions, and the dependence of N_t on IWC varies with environmental conditions at the same T.

The findings presented here apply only to data collected in the vicinity of Cayenne, French Guiana during HAIC-HIWC. Future studies should concentrate on analysis of data collected in more diverse geographic locations, and should seek to obtain more data in updrafts and downdrafts where there are still little data. Such data would permit better statistical analysis of how the microphysical characteristics of HIWC clouds vary with a range of environmental conditions to provide further insight into the microphysical processes that occur in tropical ice clouds. Model simulations evaluated with the HAIC-HIWC data can also provide this insight because applying different microphysical parameterizations in the model makes it possible to investigate the microphysical processes that are most responsible for generating large amounts of small ice crystals (e.g., Huang et al. 2021). Extending the analysis presented here to retrievals of IWC from dual-polarization radar data (X and

W bands) evaluated against in situ data acquired during the project can also extend the amount of data available for the analysis (Nguyen et al. 2019).

Acknowledgments. This work was supported by the National Science Foundation (Awards 1213311 and 1842094). Observation data are provided through NCAR/EOL under the sponsorship of the National Science Foundation (https://data.eol.ucar.edu/). NCAR is sponsored by the National Science Foundation. Major North American funding for flight campaigns was provided by the FAA William Hughes Technical Center and Aviation Weather Research Program, the NASA Aeronautics Research Mission Directorate Aviation Safety Program, the Boeing Co., Environment and Climate Change Canada, the National Research Council of Canada, and Transport Canada. Major European campaign and research funding was provided from (i) the European Commission Seventh Framework Program in research, technological development, and demonstration under Grant ACP2-GA-2012-314314, (ii) the European Safety Agency (EASA) Research Program under Service Contract EASA.2013.FC27. Operational support for the research aircraft Falcon 20 was provided by the SAFIRE facility for the scientific airborne operations. SAFIRE (http://www.safire.fr) is a joint facility of CNRS, Météo-France and CNES. Further funding was provided by the Ice Crystal Consortium. Some of the computing for this project was performed at the University of Oklahoma (OU) Supercomputing Center for Education and Research (OSCER). The discussions of HIWC conditions and aircraft measurements with Walter Strapp are greatly appreciated. The first author is also supported by the China Scholarship Council (CSC). The authors are also grateful to three anonymous reviewers who provided helpful comments and suggestions that improved the manuscript.

REFERENCES

Ackerman, S. A., 1996: Global satellite observations of negative brightness temperature differences between 11 and 6.7 μm. *J. Atmos. Sci.*, **53**, 2803–2812, https://doi.org/10.1175/1520-0469(1996)053<2803:GSOONB>2.0.CO;2.

Ai, Y. F., W. B. Li, Z. Y. Meng, and J. Li, 2016: Life cycle characteristics of MCSs in middle east China tracked by geostationary satellite and precipitation estimates. *Mon. Wea. Rev.*, **144**, 2517–2530, https://doi.org/10.1175/MWR-D-15-0197.1.

Arkin, P. A., and B. N. Meisner, 1987: The relationship between large-scale convective rainfall and cold cloud over the Western Hemisphere during 1982–84. *Mon. Wea. Rev.*, **115**, 51–74, https://doi.org/10.1175/1520-0493(1987)115<0051:TRBLSC>2.0.CO;2.

Baumgardner, D., and A. Rodi, 1989: Laboratory and wind tunnel evaluations of the Rosemount Icing Detector. *J. Atmos. Oceanic Technol.*, **6**, 971–979, https://doi.org/10.1175/1520-0426(1989)006<0971:LAWTEO>2.0.CO;2.

——, and A. Korolev, 1997: Airspeed corrections for optical array probe sample volumes. *J. Atmos. Oceanic Technol.*, **14**, 1224–1229, https://doi.org/10.1175/1520-0426(1997)014<1224:ACFOAP>2.0.CO;2.

——, and Coauthors, 2011: Airborne instruments to measure atmospheric aerosol particles, clouds and radiation: A cook's tour of mature and emerging technology. *Atmos. Res.*, **102**, 10–29, https://doi.org/10.1016/j.atmosres.2011.06.021.

——, and Coauthors, 2017: Cloud ice properties: In situ measurement challenges. *Ice Formation and Evolution in Clouds and Precipitation: Measurement and Modeling Challenges*, *Meteor. Monogr.*, No. 58, Amer. Meteor. Soc., 9.1–9.23, https://doi.org/10.1175/AMSMONOGRAPHS-D-16-0011.1.

Boudala, F. S., G. A. Isaac, N. A. McFarlane, and J. Li, 2007: The sensitivity of the radiation budget in a climate simulation to neglecting the effect of small ice particles. *J. Climate*, **20**, 3527–3541, https://doi.org/10.1175/JCLI4191.1.

Bouniol, D., J. Delanoë, C. Duroure, A. Protat, V. Giraud, and G. Penide, 2010: Microphysical characterization of West African MCS anvils. *Quart. J. Roy. Meteor. Soc.*, **136**, 323–344, https://doi.org/10.1002/qj.557.

——, R. Roca, T. Fiolleau, and D. E. Poan, 2016: Macrophysical, microphysical, and radiative properties of tropical mesoscale convective systems over their life cycle. *J. Climate*, **29**, 3353–3371, https://doi.org/10.1175/JCLI-D-15-0551.1.

Bravin, M., J. W. Strapp, and J. Mason, 2015: An investigation into location and convective lifecycle trends in an ice crystal icing engine database. Tech. Rep., SAE Tech. Paper, 8 pp.

Chen, D., J. Guo, H. Wang, J. Li, M. Min, W. Zhao, and D. Yao, 2018: The cloud top distribution and diurnal variation of clouds over East Asia: Preliminary results from Advanced Himawari Imager. *J. Geophys. Res. Atmos.*, **123**, 3724–3739, https://doi.org/10.1002/2017JD028044.

Chopde, N. R., and M. Nichat, 2013: Landmark based shortest path detection by using A* and Haversine formula. *Int. J. Innov. Res. Comput. Commun. Eng.*, **1**, 298–302.

Cifelli, R., T. Lang, S. A. Rutledge, N. Guy, E. J. Zipser, J. Zawislak, and R. Holzworth, 2010: Characteristics of an African easterly wave observed during NAMMA. *J. Atmos. Sci.*, **67**, 3–25, https://doi.org/10.1175/2009JAS3141.1.

Claffey, K. J., K. F. Jones, and C. C. Ryerson, 1995: Use and calibration of Rosemount ice detectors for meteorological research. *Atmos. Res.*, **36**, 277–286, https://doi.org/10.1016/0169-8095(94)00042-C.

Cober, S. G., G. A. Isaac, and A. V. Korolev, 2001: Assessing the Rosemount Icing Detector with in situ measurements. *J. Atmos. Oceanic Technol.*, **18**, 515–528, https://doi.org/10.1175/1520-0426(2001)018<0515:ATRIDW>2.0.CO;2.

Cooper, W. A., 1986: Ice initiation in natural clouds. *Precipitation Enhancement—A Scientific Challenge*, *Meteor. Monogr.*, No. 43, Amer. Meteor. Soc., 29–32,https://doi.org/10.1175/0065-9401-21.43.29.

Cotton, R. J., and Coauthors, 2013: The effective density of small ice particles obtained from in situ aircraft observations of mid-latitude cirrus. *Quart. J. Roy. Meteor. Soc.*, **139**, 1923–1934, https://doi.org/10.1002/qj.2058.

Davison, C. R., J. MacLeod, J. Strapp, and D. Buttsworth, 2008: Isokinetic total water content probe in a naturally aspirating configuration: Initial aerodynamic design and testing. *Proc. 46th AIAA Aerospace Sciences Meeting and Exhibit*, Reno, NV, American Institute of Aeronautics and Astronautics, AIAA-2008-435, https://doi.org/10.2514/6.2008-435.

——, J. W. Strapp, L. E. Lilie, T. P. Ratvasky, and C. Dumont, 2016: Isokinetic TWC evaporator probe: Calculations and systemic error analysis. *Proc. Eighth AIAA Atmospheric and Space Envrionments Conf.*, Washington, DC, American Institute of Aeronautics and Astronautics, AIAA-2016-4060, https://doi.org/10.2514/6.2016-4060.

DeMott, P. J., and Coauthors, 2010: Predicting global atmospheric ice nuclei distributions and their impacts on climate. *Proc. Natl. Acad. Sci. USA*, **107**, 11 217–11 222, https://doi.org/10.1073/pnas.0910818107.

Dezitter, F., A. Grandin, J. L. Brenguier, F. Hervy, H. Schlager, P. Villedieu, and G. Zalamansky, 2013: HAIC (High altitude ice crystals). *Proc. Fifth AIAA Atmospheric and Space Environments Conf.*, San Diego, CA, American Institute of Aeronautics and Astronautics, AIAA-2013-2674, https://doi.org/10.2514/6.2013-2674.

Ding, S., G. M. McFarquhar, S. W. Nesbitt, R. J. Chase, M. R. Poellot, and H. Wang, 2020: Dependence of mass—Dimensional relationships on median mass diameter. *Atmosphere*, **11**, 756, https://doi.org/10.3390/atmos11070756.

Donovan, M. F., E. R. Williams, C. Kessinger, G. Blackburn, P. H. Herzegh, R. L. Bankert, S. Miller, and F. R. Mosher, 2008: The identification and verification of hazardous convective cells over oceans using visible and infrared satellite observations. *J. Appl. Meteor. Climatol.*, **47**, 164–184, https://doi.org/10.1175/2007JAMC1471.1.

Field, P. R., A. J. Heymsfield, and A. Bansemer, 2006: Shattering and particle interarrival times measured by optical array probes in ice clouds. *J. Atmos. Oceanic Technol.*, **23**, 1357–1371, https://doi.org/10.1175/JTECH1922.1.

Fletcher, N. H., 2011: *The Physics of Rainclouds*. Cambridge University Press, 410 pp., https://cds.cern.ch/record/2051935.

Fontaine, E., A. Schwarzenboeck, J. Delanoë, W. Wobrock, D. Leroy, R. Dupuy, C. Gourbeyre, and A. Protat, 2014: Constraining mass–diameter relations from hydrometeor images and cloud radar reflectivities in tropical continental and oceanic convective anvils. *Atmos. Chem. Phys.*, **14**, 11 367–11 392, https://doi.org/10.5194/acp-14-11367-2014.

——, and Coauthors, 2017: Evaluation of radar reflectivity factor simulations of ice crystal populations from in situ observations for the retrieval of condensed water content in tropical mesoscale convective systems. *Atmos. Meas. Tech.*, **10**, 2239–2252, https://doi.org/10.5194/amt-10-2239-2017.

Formenti, P., and Coauthors, 2001: Saharan dust in Brazil and Suriname during the Large-Scale Biosphere-Atmosphere Experiment in Amazonia (LBA)-Cooperative LBA Regional Experiment (CLAIRE) in March 1998. *J. Geophys. Res.*, **106**, 14 919–14 934, https://doi.org/10.1029/2000JD900827.

Franklin, C. N., A. Protat, D. Leroy, and E. Fontaine, 2016: Controls on phase composition and ice water content in a convection-permitting model simulation of a tropical mesoscale convective system. *Atmos. Chem. Phys.*, **16**, 8767–8789, https://doi.org/10.5194/acp-16-8767-2016.

Fridlind, A., A. Ackerman, A. Grandin, F. Dezitter, M. Weber, J. Strapp, A. Korolev, and C. Williams, 2015: High ice water content at low radar reflectivity near deep convection—Part 1: Consistency of in situ and remote-sensing observations with stratiform rain column simulations. *Atmos. Chem. Phys.*, **15**, 11 713–11 728, https://doi.org/10.5194/acp-15-11713-2015.

Fritz, S., and I. Laszlo, 1993: Detection of water vapor in the stratosphere over very high clouds in the tropics. *J. Geophys. Res.*, **98**, 22 959–22 967, https://doi.org/10.1029/93JD01617.

Gage, K. S., C. R. Williams, W. L. Ecklund, and P. E. Johnstonb, 1999: Development and application of Doppler radar profilers to ground validation of satellite precipitation measurements. *Adv. Space Res.*, **24**, 931–934, https://doi.org/10.1016/S0273-1177(99)00366-X.

Gonzalez, R. C., S. L. Eddins, and R. E. Woods, 2004: *Digital Image Publishing Using MATLAB*. Prentice Hall, 609 pp.

Grandin, A., J. M. Merle, M. Weber, J. Strapp, A. Protat, and P. King, 2014: AIRBUS flight tests in high total water content regions. *Proc. Sixth AIAA Atmospheric and Space Environments Conf.*, Atlanta, GA, American Institute of Aeronautics and Astronautics, AIAA-2014-2753, https://doi.org/10.2514/6.2014-2753.

Halverson, J., and Coauthors, 2007: NASA's tropical cloud systems and processes experiment: Investigating tropical cyclogenesis and hurricane intensity change. *Bull. Amer. Meteor. Soc.*, **88**, 867–882, https://doi.org/10.1175/BAMS-88-6-867.

Hartmann, J., M. Gehrmann, K. Kohnert, S. Metzger, and T. Sachs, 2018: New calibration procedures for airborne turbulence measurements and accuracy of the methane fluxes during the AirMeth campaigns. *Atmos. Meas. Tech.*, **11**, 4567–4581, https://doi.org/10.5194/amt-11-4567-2018.

Heymsfield, A. J., and J. L. Parrish, 1978: A computational technique for increasing the effective sampling volume of the PMS two-dimensional particle size spectrometer. *J. Appl. Meteor.*, **17**, 1566–1572, https://doi.org/10.1175/1520-0450(1978)017<1566:ACTFIT>2.0.CO;2.

——, and G. M. McFarquhar, 2002: Mid-latitude and tropical cirrus: Microphysical properties. *Cirrus*, D. K. Lynch et al., Eds., Oxford University Press, https://doi.org/10.1093/oso/9780195130720.003.0008.

——, A. Bansemer, P. R. Field, S. L. Durden, J. L. Stith, J. E. Dye, W. Hall, and C. A. Grainger, 2002: Observations and parameterizations of particle size distributions in deep tropical cirrus and stratiform precipitating clouds: Results from in situ observations in TRMM field campaigns. *J. Atmos. Sci.*, **59**, 3457–3491, https://doi.org/10.1175/1520-0469(2002)059<3457:OAPOPS>2.0.CO;2.

——, ——, C. Schmitt, C. Twohy, and M. R. Poellot, 2004: Effective ice particle densities derived from aircraft data. *J. Atmos. Sci.*, **61**, 982–1003, https://doi.org/10.1175/1520-0469(2004)061<0982:EIPDDF>2.0.CO;2.

——, ——, G. M. Heymsfield, and A. O. Fierro, 2009: Microphysics of maritime tropical convective updrafts at temperatures from −20° to −60°C. *J. Atmos. Sci.*, **66**, 3530–3562, https://doi.org/10.1175/2009JAS3107.1.

——, C. Schmitt, A. Bansemer, and C. H. Twohy, 2010: Improved representation of ice particle masses based on observations in natural clouds. *J. Atmos. Sci.*, **67**, 3303–3318, https://doi.org/10.1175/2010JAS3507.1.

——, ——, and ——, 2013: Ice cloud particle size distributions and pressure-dependent terminal velocities from in situ observations at temperatures from 0° to −86°C. *J. Atmos. Sci.*, **70**, 4123–4154, https://doi.org/10.1175/JAS-D-12-0124.1.

Hodges, K., and C. Thorncroft, 1997: Distribution and statistics of the African mesoscale convective systems based on the ISCCP Meteosat imagery. *Mon. Wea. Rev.*, **125**, 2821–2837, https://doi.org/10.1175/1520-0493(1997)125<2821:DASOAM>2.0.CO;2.

Houze, R. A., Jr., 2004: Mesoscale convective systems. *Rev. Geophys.*, **42**, RG4003, https://doi.org/10.1029/2004RG000150.

——., 2014: *Cloud Dynamics*. 2nd ed. International Geophysics Series, Vol. 104, Elsevier, 496 pp.

——., J. Wang, J. Fan, S. Brodzik, and Z. Feng, 2019: Extreme convective storms over high-latitude continental areas where maximum warming is occurring. *Geophys. Res. Lett.*, **46**, 4059–4065, https://doi.org/10.1029/2019GL082414.

Huang, Y., and Coauthors, 2021: Microphysical processes producing high ice water contents (HIWCs) in tropical convective clouds during the HAIC-HIWC field campaign: Evaluation of simulations using bulk microphysical schemes. *Atmos. Chem. Phys.*, **21**, 6919–6944, https://doi.org/10.5194/acp-21-6919-2021.

IPCC, 2013: *Climate Change 2013: The Physical Science Basis*. Cambridge University Press, 1535 pp., https://doi.org/10.1017/CBO9781107415324 .

Jackson, R. C., G. M. McFarquhar, A. M. Fridlind, and R. Atlas, 2015: The dependence of cirrus gamma size distributions expressed as volumes in N_0-λ-μ phase space and bulk cloud properties on environmental conditions: Results from the Small Ice Particles in Cirrus Experiment (SPARTICUS). *J. Geophys. Res. Atmos.*, **120**, 10 351–10 377, https://doi.org/10.1002/2015JD023492.

Jakob, C., and S. A. Klein, 1999: The role of vertically varying cloud fraction in the parametrization of microphysical processes in the ECMWF model. *Quart. J. Roy. Meteor. Soc.*, **125**, 941–965, https://doi.org/10.1002/qj.49712555510.

Jensen, E. J., and Coauthors, 2009: On the importance of small ice crystals in tropical anvil cirrus. *Atmos. Chem. Phys.*, **9**, 5519–5537, https://doi.org/10.5194/acp-9-5519-2009.

Jorgensen, D. P., E. J. Zipser, and M. A. LeMone, 1985: Vertical motions in intense hurricanes. *J. Atmos. Sci.*, **42**, 839–856, https://doi.org/10.1175/1520-0469(1985)042<0839:VMIIH>2.0.CO;2.

Kakar, R., M. Goodman, R. Hood, and A. Guillory, 2006: Overview of the Convection and Moisture Experiment (CAMEX). *J. Atmos. Sci.*, **63**, 5–18, https://doi.org/10.1175/JAS3607.1.

Kolios, S., and H. Feidas, 2010: A warm season climatology of mesoscale convective systems in the Mediterranean basin using satellite data. *Theor. Appl. Climatol.*, **102**, 29–42, https://doi.org/10.1007/s00704-009-0241-7.

Korolev, A. V., 2007: Limitations of the Wegener–Bergeron–Findeisen mechanism in the evolution of mixed-phase clouds. *J. Atmos. Sci.*, **64**, 3372–3375, https://doi.org/10.1175/JAS4035.1.

——, and P. R. Field, 2015: Assessment of performance of the inter-arrival time algorithm to identify ice shattering artifacts in cloud particle probes measurements. *Atmos. Meas. Tech.*, **8**, 761–777, https://doi.org/10.5194/amt-8-761-2015.

——, J. W. Strapp, G. A. Isaac, and A. N. Nevzorov, 1998: The Nevzorov airborne hot-wire LWC–TWC probe: Principle of operation and performance characteristics. *J. Atmos. Oceanic Technol.*, **15**, 1495–1510, https://doi.org/10.1175/1520-0426(1998)015<1495:TNAHWL>2.0.CO;2.

——, E. F. Emery, J. W. Strapp, S. G. Cober, G. A. Isaac, M. Wasey, and D. Marcotte, 2011: Small ice particles in tropospheric clouds: Fact or artifact? Airborne Icing Instrumentation Evaluation Experiment. *Bull. Amer. Meteor. Soc.*, **92**, 967–973, https://doi.org/10.1175/2010BAMS3141.1.

——, ——, and K. Creelman, 2013a: Modification and tests of particle probe tips to mitigate effects of ice shattering. *J. Atmos. Oceanic Technol.*, **30**, 690–708, https://doi.org/10.1175/JTECH-D-12-00142.1.

——, ——, J. W. Strapp, S. G. Cober, and G. A. Isaac, 2013b: Quantification of the effects of shattering on airborne ice particle measurements. *J. Atmos. Oceanic Technol.*, **30**, 2527–2553, https://doi.org/10.1175/JTECH-D-13-00115.1.

——, I. Heckman, and M. Wolde, 2018: Observation of phase composition and humidity in oceanic mesoscale convective systems. *15th Conf. on Cloud Physics*, Vancouver, BC, Canada, Amer. Meteor. Soc., 236, https://ams.confex.com/ams/15CLOUD15ATRAD/webprogram/Paper347111.html.

——, and Coauthors, 2020: A new look at the environmental conditions favorable to secondary ice production. *Atmos. Chem. Phys.*, **20**, 1391–1429, https://doi.org/10.5194/acp-20-1391-2020.

Krämer, M., and Coauthors, 2009: Ice supersaturations and cirrus cloud crystal numbers. *Atmos. Chem. Phys.*, **9**, 3505–3522, https://doi.org/10.5194/acp-9-3505-2009.

Lance, S., C. A. Brock, D. Rogers, and J. A. Gordon, 2010: Water droplet calibration of the Cloud Droplet Probe (CDP) and in-flight performance in liquid, ice and mixed-phase clouds during ARCPAC. *Atmos. Meas. Tech.*, **3**, 1683–1706, https://doi.org/10.5194/amt-3-1683-2010.

Laurent, H., L. Machado, C. Morales, and L. Durieux, 2002: Characteristics of the Amazonian mesoscale convective systems observed from satellite and radar during the WETAMC/LBA experiment. *J. Geophys. Res.*, **107**, 8054, https://doi.org/10.1029/2001JD000337.

Lawson, R. P., L. J. Angus, and A. J. Heymsfield, 1998: Cloud particle measurements in thunderstorm anvils and possible weather threat to aviation. *J. Aircr.*, **35**, 113–121, https://doi.org/10.2514/2.2268.

——, D. O'Connor, P. Zmarzly, K.Weaver, B. Baker, Q. Mo, and H. Jonsson, 2006: The 2D-S (stereo) probe: Design and preliminary tests of a new airborne, high-speed, high-resolution particle imaging probe. *J. Atmos. Oceanic Technol.*, **23**, 1462–1477, https://doi.org/10.1175/JTECH1927.1.

——, E. Jensen, D. L. Mitchell, B. Barker, Q. Mo, and B. Pilson, 2010: Microphysical and radiative properties of tropical clouds investigated in TC4 and NAMMA. *J. Geophys. Res.*, **115**, D00J08, https://doi.org/10.1029/2009JD013017.

Leary, C. A., and R. A. Houze, 1980: The contribution of mesoscale motions to the mass and heat fluxes of an intense tropical convective system. *J. Atmos. Sci.*, **37**, 784–796, https://doi.org/10.1175/1520-0469(1980)037<0784:TCOMMT>2.0.CO;2.

Leroy, D., and Coauthors, 2016a: HAIC/HIWC field campaigns—Specific findings on ice crystals characteristics in high ice water content cloud regions. *Proc. Eighth AIAA Atmospheric and Space Environments Conf.*, Washington, DC, American Institute of Aeronautics and Astronautics, AIAA 2016-4056, https://doi.org/10.2514/6.2016-4056.

——, E. Fontaine, A. Schwarzenboeck, and J. W. Strapp, 2016b: Ice crystal sizes in high ice water content clouds. Part I: On the computation of median mass diameters from in situ measurements. *J. Atmos. Oceanic Technol.*, **33**, 2461–2476, https://doi.org/10.1175/JTECH-D-15-0151.1.

——, and Coauthors, 2017: Ice crystal sizes in high ice water content clouds. Part II: Statistics of mass diameter percentiles in tropical convection observed during the HAIC/HIWC project. *J. Atmos. Oceanic Technol.*, **34**, 117–136, https://doi.org/10.1175/JTECH-D-15-0246.1.

Levizzani, V., and M. Setvák, 1996: Multispectral, high-resolution satellite observations of plumes on top of convective storms. *J. Atmos. Sci.*, **53**, 361–369, https://doi.org/10.1175/1520-0469(1996)053<0361:MHRSOO>2.0.CO;2.

Lilly, D. K., 1988: Cirrus outflow dynamics. *J. Atmos. Sci.*, **45**, 1594–1605, https://doi.org/10.1175/1520-0469(1988)045<1594:COD>2.0.CO;2.

Lucas, C., E. J. Zipser, and M. A. Lemone, 1994: Vertical velocity in oceanic convection off tropical Australia. *J. Atmos. Sci.*, **51**, 3183–3193, https://doi.org/10.1175/1520-0469(1994)051<3183:VVIOCO>2.0.CO;2.

Machado, L. A. T., W. B. Rossow, R. L. Guedes, and A. W. Walker, 1998: Life cycle variations of mesoscale convective systems over the Americas. *Mon. Wea. Rev.*, **126**, 1630–1654, https://doi.org/10.1175/1520-0493(1998)126<1630:LCVOMC>2.0.CO;2.

Markowski, P., and Y. Richardson, 2010: *Mesoscale Meteorology in Midlatitudes.* Wiley, 430 pp.

Mascio, J., G. M. McFarquhar, T. Hsieh, M. Freer, A. Dooley, and A. J. Heymsfield, 2020: The use of gamma distributions to quantify the dependence of cloud particle size distributions in hurricanes on cloud and environmental conditions. *Quart.*

J. Roy. Meteor. Soc., **146**, 2116–2137, https://doi.org/10.1002/qj.3782.

Mason, J., W. Strapp, and P. Chow, 2006: The ice particle threat to engines in flight. *Proc. 44th AIAA Aerospace Sciences Meeting and Exhibit*, Reno, NV, American Institute of Aeronautics and Astronautics, AIAA-2006-206, https://doi.org/10.2514/6.2006-206.

Matsui, T., J. Chern, W. Tao, S. Lang, M. Satoh, T. Hashino, and T. Kubota, 2016: On the land–ocean contrast of tropical convection and microphysics statistics derived from TRMM satellite signals and global storm-resolving models. *J. Hydrometeor.*, **17**, 1425–1445, https://doi.org/10.1175/JHM-D-15-0111.1.

May, P. T., J. H. Mather, G. Vaughan, C. Jakob, G. M. McFarquhar, K. N. Bower, and G. G. Mace, 2008: The Tropical Warm Pool International Cloud Experiment. *Bull. Amer. Meteor. Soc.*, **89**, 629–646, https://doi.org/10.1175/BAMS-89-5-629.

Mazin, I. P., A. V. Korolev, A. Heymsfield, G. A. Isaac, and S. G. Cober, 2001: Thermodynamics of icing cylinder for measurements of liquid water content in supercooled clouds. *J. Atmos. Oceanic Technol.*, **18**, 543–558, https://doi.org/10.1175/1520-0426(2001)018<0543:TOICFM>2.0.CO;2.

McFarquhar, G. M., and A. J. Heymsfield, 1996: Microphysical characteristics of three anvils sampled during the Central Equatorial Pacific Experiment. *J. Atmos. Sci.*, **53**, 2401–2423, https://doi.org/10.1175/1520-0469(1996)053<2401:MCOTAS>2.0.CO;2.

——, and R. A. Black, 2004: Observations of particle size and phase in tropical cyclones: Implications for mesoscale modeling of microphysical processes. *J. Atmos. Sci.*, **61**, 422–439, https://doi.org/10.1175/1520-0469(2004)061<0422:OOPSAP>2.0.CO;2.

——, A. J. Heymsfield, J. Spinhirne, and B. Hart, 2000: Thin and subvisual tropopause tropical cirrus: Observations and radiative impacts. *J. Atmos. Sci.*, **57**, 1841–1853, https://doi.org/10.1175/1520-0469(2000)057<1841:TASTTC>2.0.CO;2.

——, S. Iacobellis, and R. C. J. Somerville, 2003: SCM simulations of tropical ice clouds using observationally based parameterizations of microphysics. *J. Climate*, **16**, 1643–1664, https://doi.org/10.1175/1520-0442(2003)016<1643:SSOTIC>2.0.CO;2.

——, J. Um, M. Freer, D. Baumgardner, G. L. Kok, and G. Mace, 2007a: Importance of small ice crystals to cirrus properties: Observations from the Tropical Warm Pool International Cloud Experiment (TWP-ICE). *Geophys. Res. Lett.*, **34**, L13803, https://doi.org/10.1029/2007GL029865.

——, M. S. Timlin, R. M. Rauber, B. F. Jewett, J. A. Grim, and D. P. Jorgensen, 2007b: Vertical variability of cloud hydrometeors in the stratiform region of mesoscale convective systems and bow echoes. *Mon. Wea. Rev.*, **135**, 3405–3428, https://doi.org/10.1175/MWR3444.1.

——, and Coauthors, 2017: Processing of ice cloud in situ data collected by bulk water, scattering, and imaging probes: Fundamentals, uncertainties, and efforts towards consistency. *Ice Formation and Evolution in Clouds and Precipitation: Measurement and Modeling Challenges*, *Meteor. Monogr.*, No. 58, Amer. Meteor. Soc., 11.1–11.33, https://doi.org/10.1175/AMSMONOGRAPHS-D-16-0007.1.

Meyers, M. P., P. J. DeMott, and W. R. Cotton, 1992: New primary ice-nucleation parameterizations in an explicit cloud model. *J. Appl. Meteor.*, **31**, 708–721, https://doi.org/10.1175/1520-0450(1992)031<0708:NPINPI>2.0.CO;2.

Mitchell, D. L., P. Rasch, D. Ivanova, G. McFarquhar, and T. Nousiainen, 2008: Impact of small ice crystal assumptions on ice sedimentation rates in cirrus clouds and GCM simulations. *Geophys. Res. Lett.*, **35**, L09806, https://doi.org/10.1029/2008GL033552.

Muhlbauer, A., T. P. Ackerman, J. M. Comstock, G. S. Diskin, S. M. Evans, R. P. Lawson, and R. T. Marchand, 2014: Impact of large-scale dynamics on the microphysical properties of midlatitude cirrus. *J. Geophys. Res. Atmos.*, **119**, 3976–3996, https://doi.org/10.1002/2013JD020035.

Murphy, A. M., R. M. Rauber, G. M. McFarquhar, J. A. Finlon, D. M. Plummer, A. A. Rosenow, and B. F. Jewett, 2017: A microphysical analysis of elevated convection in the comma head region of continental winter cyclones. *J. Atmos. Sci.*, **74**, 69–91, https://doi.org/10.1175/JAS-D-16-0204.1.

Nguyen, C. M., M. Wolde, and A. Korolev, 2019: Determination of ice water content (IWC) in tropical convective clouds from X-band dual-polarization airborne radar. *Atmos. Meas. Tech.*, **12**, 5897–5911, https://doi.org/10.5194/amt-12-5897-2019.

Nieman, S. J., W. P. Menzei, C. M. Hayden, D. Gray, S. T. Wanzong, C. S. Velden, and J. Daniels, 1997: Fully automated cloud-drift winds in NESDIS operations. *Bull. Amer. Meteor. Soc.*, **78**, 1121–1134, https://doi.org/10.1175/1520-0477(1997)078<1121:FACDWI>2.0.CO;2.

Protat, A., and Coauthors, 2009: Assessment of *CloudSat* reflectivity measurements and ice cloud properties using ground-based and airborne cloud radar observations. *J. Atmos. Oceanic Technol.*, **26**, 1717–1741, https://doi.org/10.1175/2009JTECHA1246.1.

Rafati, S., and M. Karimi, 2017: Assessment of mesoscale convective systems using IR brightness temperature in the southwest of Iran. *Theor. Appl. Climatol.*, **129**, 539–549, https://doi.org/10.1007/s00704-016-1797-7.

Ratvasky, T. P., and Coauthors, 2019: Summary of the high ice water content (HIWC) RADAR flight campaigns, Tech. Rep., SAE Tech. Paper, 36 pp.

Sanderson, B. M., C. Piani, W. J. Ingram, D. A. Stone, and M. R. Allen, 2008: Towards constraining climate sensitivity by linear analysis of feedback patterns in thousands of perturbed-physics GCM simulations. *Climate Dyn.*, **30**, 175–190, https://doi.org/10.1007/s00382-007-0280-7.

Sobel, A. H., S. E. Yuter, C. S. Bretherton, and G. N. Kiladis, 2004: Large-scale meteorology and deep convection during TRMM KWAJEX. *Mon. Wea. Rev.*, **132**, 422–444, https://doi.org/10.1175/1520-0493(2004)132<0422:LMADCD>2.0.CO;2.

Stanford, M. W., A. Varble, E. Zipser, J. W. Strapp, D. Leroy, A. Schwarzenboeck, R. Potts, and A. Protat, 2017: A ubiquitous ice size bias in simulations of tropical deep convection. *Atmos. Chem. Phys.*, **17**, 9599–9621, https://doi.org/10.5194/acp-17-9599-2017.

Stephens, G. L., 2005: Cloud feedbacks in the climate system: A critical review. *J. Climate*, **18**, 237–273, https://doi.org/10.1175/JCLI-3243.1.

Strapp, J. W., J. MacLeod, and L. Lilie, 2008: Calibration of ice water content in a wind tunnel/engine test cell facility. *Extended Abstracts*, *15th Int. Conf. on Cloud and Precipitation*, Cancun, MX, International Commission on Clouds and Precipation, P13.1, http://cabernet. atmosfcu.unam.mx/ICCP-2008/abstracts/Program_on_line/ Poster_13/StrappEtAl-extended.pdf.

——, L. E. Lilie, T. P. Ratvasky, C. R. Davison, and C. Dumont, 2016a: Isokinetic TWC evaporator probe: Development of the IKP2 and performance testing for the HAIC-HIWC Darwin 2014 and Cayenne field campaigns. *Proc. Eighth AIAA Atmospheric and Space Environments Conf.*, Washington,

DC, American Institute of Aeronautics and Astronautics, AIAA-2016-4059, https://doi.org/10.2514/6.2016-4059.

——, and Coauthors, 2016b: The high ice water content (HIWC) study of deep convective clouds: Science and technical plan. FAA Rep., DOT/FAA/TC-14/31, 105 pp.

——, and Coauthors, 2020: An assessment of cloud total water content and particle size from flight test campaign measurements in high ice water content, mixed phase/ice crystal icing conditions: Primary in-situ measurements. FAA Rep., DOT/FAA/TC-18/1, 262 pp.

——, and Coauthors, 2021: Comparisons of cloud in situ microphysical properties of deep convective clouds to appendix D/P using data from the high-altitude ice crystals-high ice water content and high ice water content-RADAR I flight campaigns. *SAE Int. J. Aerosp.*, **14**, https://doi.org/10.4271/01-14-02-0007.

Toon, O. B., and Coauthors, 2010: Planning, implementation, and first results of the Tropical Composition, Cloud and Climate Coupling Experiment (TC4). *J. Geophys. Res.*, **115**, D00J04, https://doi.org/10.1029/2009JD013073.

Velden, C. S., C. M. Hayden, S. J. Nieman, W. P. Menzel, S. Wanzong, and J. S. Goerss, 1997: Upper-tropospheric winds derived from geostationary satellite water vapor observations. *Bull. Amer. Meteor. Soc.*, **78**, 173–195, https://doi.org/10.1175/1520-0477(1997)078<0173:UTWDFG>2.0.CO;2.

Vila, D. A., L. A. T. Machado, H. Laurent, and I. Velasco, 2008: Forecast and tracking the evolution of cloud clusters (ForTraCC) using satellite infrared imagery: Methodology and validation. *Wea. Forecasting*, **23**, 233–245, https://doi.org/10.1175/2007WAF2006121.1.

Wolde, M., and A. Pazmany, 2005: NRC dual-frequency airborne radar for atmospheric research. *32nd Conf. on Radar Meteorology*, Albuquerque, NM, Amer. Meteor. Soc., P1R.9, https://ams.confex.com/ams/32Rad11Meso/techprogram/paper_96918.htm.

——, C. Nguyen, A. Korolev, and M. Bastian, 2016: Characterization of the Pilot X-band radar responses to the HIWC environment during the Cayenne HAIC-HIWC 2015 Campaign. *Proc. Eighth AIAA Atmospheric and Space Environments Conf.*, Washington, DC, American Institute of Aeronautics and Astronautics, AIAA 2016-4201, https://doi.org/10.2514/6.2016-4201.

Wu, Q., H. Wang, Y. Lin, Y. Zhuang, and Y. Zhang, 2016: Deriving AMVs from geostationary satellite images using optical flow algorithm based on polynomial expansion. *J. Atmos. Oceanic Technol.*, **33**, 1727–1747, https://doi.org/10.1175/JTECH-D-16-0013.1.

Yost, C. R., and Coauthors, 2018: A prototype method for diagnosing high ice water content probability using satellite imager data. *Atmos. Meas. Tech.*, **11**, 1615–1637, https://doi.org/10.5194/amt-11-1615-2018.

Zipser, E. J., C. Liu, D. J. Cecil, S. W. Nesbitt, and D. P. Yorty, 2006: Where are the most intense thunderstorms on Earth? *Bull. Amer. Meteor. Soc.*, **87**, 1057–1072, https://doi.org/10.1175/BAMS-87-8-1057.